iScience

CellPress

Article

Nanocarbon-Edge-Anchored High-Density Pt Atoms for 3-nitrostyrene Hydrogenation: Strong Metal-Carbon Interaction

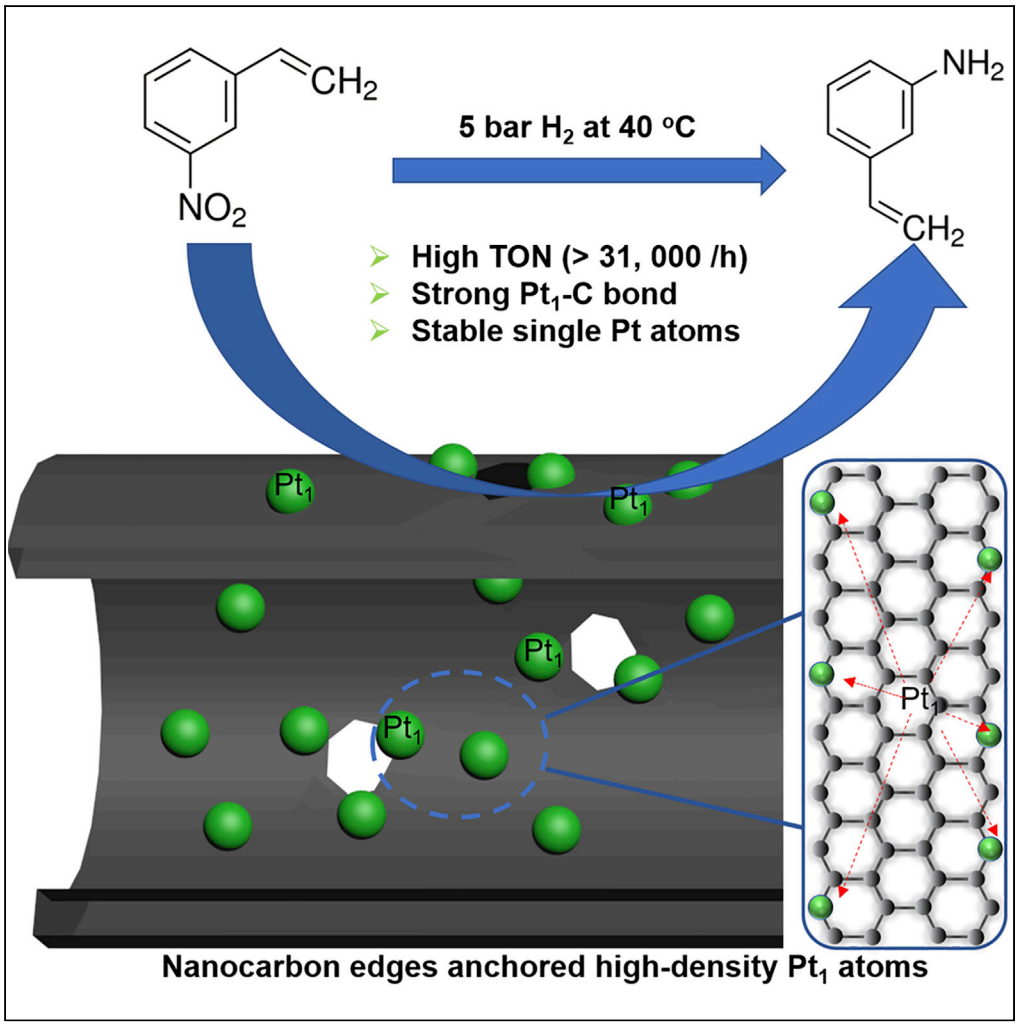

Yang Lou, Honglu Wu, Jingyue Liu

jingyue.liu@asu.edu

HIGHLIGHTS

A strategy is proposed to anchor metal atoms to edge carbon atoms of graphene sheets

Formation of Pt_1-C bond tunes performance of Pt_1/h-NC single-atom catalyst (SAC)

Pt_1/h-NC SAC is 20 times more active than the best catalyst for 3-nitrostyrene hydrogenation

Electronic SMSI can be effectively used to tune catalytic properties of SACs

Lou et al., iScience *13*, 190–198
March 29, 2019
https://doi.org/10.1016/j.isci.2019.02.016

iScience

CellPress

Article

Nanocarbon-Edge-Anchored High-Density Pt Atoms for 3-nitrostyrene Hydrogenation: Strong Metal-Carbon Interaction

Yang Lou,[1] Honglu Wu,[1] and Jingyue Liu[1,2,*]

SUMMARY

Strong metal-support interaction (SMSI) has been widely used to improve catalytic performance and to identify reaction mechanisms. We report that single Pt atoms anchored onto hollow nanocarbon (h-NC) edges possess strong metal-carbon interaction, which significantly modifies the catalytic behavior of the anchored Pt atoms for selective hydrogenation reactions. The strong Pt-C bonding not only stabilizes single Pt atoms but also modifies their electronic structure, tunes their adsorption properties, and enhances activation of reactants. The fabricated Pt_1/h-NC single-atom catalysts (SACs) demonstrated excellent activity for hydrogenation of 3-nitrostyrene to 3-vinylaniline with a turnover number >31,000/h, 20 times higher than that of the best catalyst for such selective hydrogenation reactions reported in the literature. The strategy to strongly anchor Pt atoms by edge carbon atoms of h-NCs is general and can be extended to construct strongly anchored metal atoms, via SMSI, onto surfaces of various types of support materials to develop robust SACs.

INTRODUCTION

Supported metal catalysts with metal particles finely dispersed on high-surface-area support materials are vital for many industrially important catalytic reactions. The surface physicochemical properties of the supports play a crucial role in modifying the catalytic behaviors of supported metal species via the strong metal-support interaction (SMSI) (Lee et al., 2015; Tang et al., 2016a, 2016b; Vannice, 1979; Matsubu et al., 2017). The classical SMSI phenomenon was discovered on titania-supported Pt-group metals of which high temperature reduction significantly influenced the adsorption properties of small molecules such as H_2 and CO (Tauster et al., 1978). It has been reported that pretreatment and reaction conditions induce the SMSI as well in oxides supported Au (for CO oxidation) (Liu et al., 2012) and Rh (for CO_2 reduction by H_2) catalysts (Matsubu et al., 2017), which are termed oxidative and adsorbate-mediated SMSI. Recent reports demonstrated that carbides (Dong et al., 2018), phosphates (Tang et al., 2016a, 2016b), and layered double hydroxides (Wang et al., 2017) supported Au catalysts exhibited the SMSI effects for water-gas shift, CO oxidation, and ethanol dehydrogenation reactions, respectively. The SMSI has been widely exploited to improve catalyst stability (Lee et al., 2015; Tang et al., 2016a, 2016b), identify reaction mechanisms (Matsubu et al., 2017; Bonanni et al., 2012), and enhance activity (Vannice, 1979; Sonstrom et al., 2011). It is highly desired to extend the applications of SMSI concept to broader catalyst systems, beyond metal particles, to tune catalytic properties for desirable performance.

Carbon-based catalysts have been widely used in liquid phase hydrogenation reactions because of their high chemical stability, high total surface area, and unique electronic properties (Su et al., 2017). It has been reported that the interaction between metal species and carbon surfaces can be significantly strengthened by engineering defects of, introducing functional groups to, and/or incorporating heteroatoms in carbon structures (Charlier, 2002; Lordi et al., 2001; Ebbesen and Takada, 1995). For example, single metal atoms that are anchored onto heteroatom-doped (e.g., N, O) carbon materials exhibited excellent catalytic performance for various catalytic transformations, such as methane activation (Cui et al., 2018), selective hydrogenation (Yan et al., 2015), hydrogen evolution (Fei et al., 2015; Liu et al., 2018), and oxygen reduction (Zitolo et al., 2015; Li et al., 2018). The uniformity of isolated active sites and the strong interaction between individual metal atoms and support surfaces facilitate the tuning of both selectivity and activity (Qiao et al., 2011; Liu, 2017a, 2017b; Gates et al., 2017; Wang et al., 2018; Chen et al., 2018). However, the structure of high-surface-area activated carbon supports can become

[1]Department of Physics, Arizona State University, Tempe, AZ 85287, USA

[2]Lead Contact

*Correspondence: jingyue.liu@asu.edu

https://doi.org/10.1016/j.isci.2019.02.016

extremely complex and consequently poses formidable challenges for correlating the metal-carbon interaction with the observed catalytic properties.

In this work, we fabricated hollow nanocarbons (h-NCs) that possess high-number density of surface edge/defect sites, high total surface area, and highly accessible mesopores. We anchored ~1.0 wt.% single Pt atoms to the edge/defect sites of the h-NCs to synthesize h-NC supported Pt_1 single-atom catalysts (SACs), denoted as 1.0 wt.% Pt_1/h-NC. The selective hydrogenation of 3-nitrostyrene to functionalized anilines, which are industrially key intermediates for fine chemicals (Downing et al., 1997; Corma and Serna, 2006), was chosen to probe how the SMSI between carbon and single metal atoms affects the catalytic performance of the fabricated Pt_1/h-NC SAC for liquid phase catalytic reactions. Our comprehensive characterization results indicate that the strong interaction between Pt atoms and carbon edge/defect sites modulates the electronic structure of the anchored single Pt atoms and thus their reactivity. The 1.0 wt.% Pt_1/h-NC demonstrates excellent activity for hydrogenation of 3-nitrostyrene to 3-vinylaniline with a turnover number (TON) > 31,000/h, more than 20 times higher than that of the best catalyst for such selective hydrogenation reactions reported in the literature (Wei et al., 2014).

RESULTS

Synthesis of h-NCs, Pt_1/h-NC SACs, and Control Catalysts

The h-NCs were synthesized via a catalytic decomposition and reductive evaporation process by using ZnO nanowires as catalyst/template and ethanol as feedstock (see details in Transparent Methods). The residual Zn content in the synthesized h-NCs is non-detectable (<1 ppb measured by inductively coupled plasma mass spectrometry [ICP-MS]). The fabricated h-NCs possess high total surface area (1,100 m^2/g), a tube-like morphology with inner diameters ranging from 20 to 100 nm, and lengths ranging from 1 to 20 μm (Figures 1A and S1). The wall thicknesses of the h-NCs range 2–5 nm. In addition to the large mesopores of the interior regions of the hollow tubes, the h-NCs also possess numerous small mesopores (~3.2 nm, Figure S2) on their sidewalls. Aberration-corrected scanning transmission electron microscopy (ac-STEM) images clearly revealed numerous hyper-cross-linked graphene sheets with sizes ranging from 0.5 to 3.1 nm, representing highly disordered and defective graphene-like structures (Figures 1B and S3).

A strong electrostatic adsorption method (Qiao et al., 2015) was used to disperse Pt atoms onto the h-NCs with a nominal loading of 1.0 wt.% Pt (actual loading of 0.93 wt.% by ICP-MS). High-angle annular dark-field (HAADF) imaging technique, indispensable for characterizing metal atoms in SACs (Liu, 2017a, 2017b), was used to examine the spatial distribution of Pt atoms, clusters, and/or particles. The synthesized 1.0 wt.% Pt_1/h-NC contained only isolated Pt single atoms without the presence of any Pt particles/clusters (Figures 1C and S4) in the h-NCs. By analyzing numerous ac-STEM images (Figure S4) obtained from different regions, we unambiguously concluded that the as-synthesized Pt_1/h-NC catalysts contained only isolated Pt atoms uniformly dispersed onto the surfaces of the mesoporous h-NCs. The Pt atoms preferentially decorated the edges of the hyper-cross-linked nanoscale graphene sheets (Figure 1C and 1D).

A control catalyst, consisting of 1.0 wt.% Pt nanoparticles (actual loading of 0.84 wt.% by ICP-MS) with an average size of 2.3 $\pm$ 0.1 nm dispersed onto the h-NCs (Figure S5), was synthesized and denoted as 1.0 wt.% nano-Pt/h-NC. We also synthesized another control catalyst by using the carbon black Vulcan XC-72 powders. Since the BET surface area of the XC-72 (254 m^2/g) is ~4 times lower than that of our home-made h-NCs (1,100 m^2/g), we loaded only ~0.25 wt.% of Pt (actual loading of 0.08 wt.% by ICP-MS) so that the normalized number density of surface Pt atoms is approximately the same for both the Pt/h-NC and Pt/XC-72 catalysts. The STEM images (Figure S6) show that the 0.25 wt.% Pt_1/XC-72 catalyst mainly contained atomically dispersed Pt atoms.

Catalytic Performance and Stability of the Fabricated Pt_1/h-NC SACs

Hydrogenation of 3-nitrostyrene is used to probe the catalytic properties of the synthesized catalysts. As shown in Table 1 and Figure S7, the 1.0 wt.% Pt_1/h-NC SAC is highly active with a selectivity of ~78% toward 3-vinylaniline even under very mild reaction conditions (5 bar H_2 at 40°C). The 3-ethylaniline is the only detectable by-product. For comparison, the literature reports a selectivity of <3% (toward 3-vinylaniline) on un-modified Pt/C catalysts (Corma and Serna, 2006). The TON for 3-vinylaniline was calculated to be 31,157/h (see details on kinetic data measurements in Transparent Methods), more than 20 times higher than that of the best catalyst (0.08 wt.% Pt_1/FeO_x) reported in the literature (Wei et al., 2014). Under the

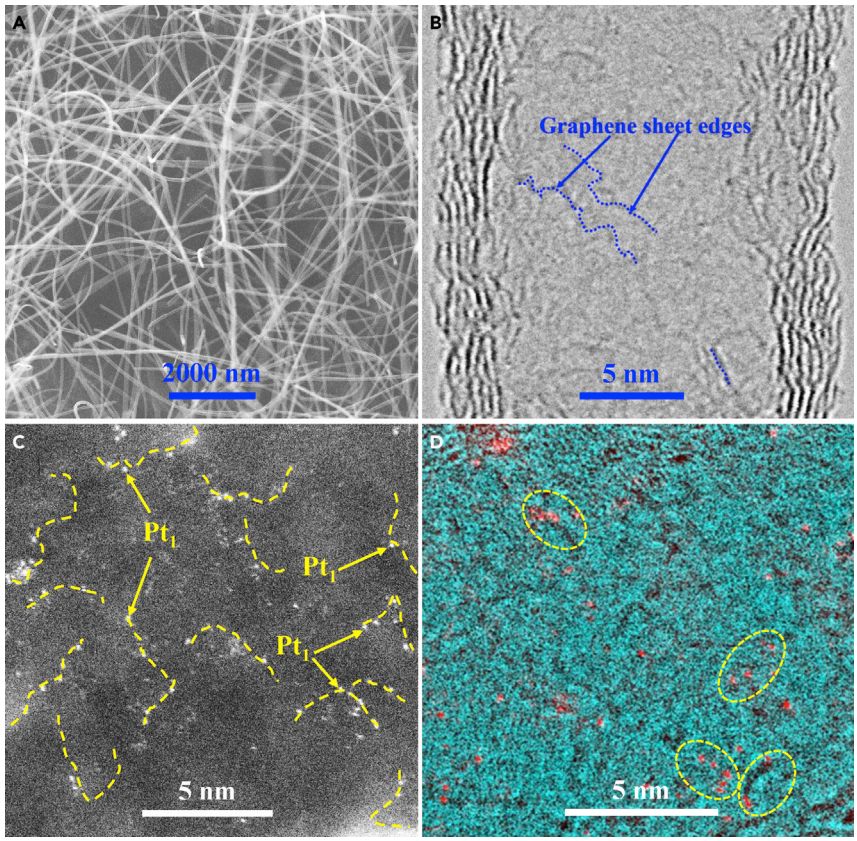

Figure 1. Electron Microscopy Images of Synthesized h-NCs and Fresh 1.0 wt.% Pt_1/h-NC SAC

(A) Scanning electron microscope image of morphology; (B) bright-field STEM image of edge/defect sites of the synthesized h-NCs; (C) high-magnification HAADF image of the fresh 1.0 wt.% Pt_1/h-NC SAC; (D) false color composite image obtained from the simultaneously acquired HAADF and bright-field STEM images to show the spatial relationship between the Pt single atoms and the nanoscale graphene sheets in the h-NCs. The scale bar sizes of Figures 1A–1D are 200, 5, 5, and 5 nm, respectively.

same reaction conditions, the 1.0 wt.% nano-Pt/h-NC yielded a dramatically decreased selectivity toward 3-vinylaniline: the products consisted of ~47% 3-vinylaniline and ~53% 3-ethylaniline, and the TON for producing 3-vinylaniline was ~2,018/h, about 15 times smaller than that of the 1.0 wt.% Pt_1/h-NC SAC. Furthermore, the presence of single Pt atoms in the 1.0 wt.% nano-Pt/h-NC catalyst (Figure S5) might have contributed to the activity and selectivity of the 1.0 wt.% nano-Pt/h-NC catalyst, suggesting that the true TON and selectivity toward 3-vinylaniline on the Pt nanoparticles may be much smaller than those of the measured values. These catalytic testing results unambiguously demonstrate that the h-NC supported single Pt atoms are much more active and selective toward 3-vinylaniline. Our experimental results clearly show that the h-NC supported Pt nanoparticles produce dominantly 3-ethylaniline (~53%), whereas the graphene-edge-anchored Pt single atoms yield dominantly 3-vinylaniline (~78%). The large differences in product selectivity manifest the intrinsically different catalytic properties of strongly anchored Pt single atoms from those of the supported Pt nanoparticles.

For the atomically dispersed 0.25 wt.% Pt_1/XC-72 control catalyst, the selectivity toward 3-vinylaniline was measured to be ~41% and the corresponding TON was 1,225/h, ~25 times lower than that on the 1.0 wt.% Pt_1/h-NC SAC. The significant changes in both the TON and selectivity implies that the catalytic property of the 1.0 wt.% Pt_1/h-NC SAC is intrinsically different from that of the atomically dispersed 0.25 wt.% Pt_1/XC-72. As clearly shown in Table 1, the TON for 3-vinylaniline on the 1.0 wt.% Pt_1/h-NC SAC is at least one order of magnitude higher than that on all other catalysts. Control experiments conducted on pure h-NC and XC-72 supports only, under the same reaction conditions, did not exhibit any detectable products.

Sample	T/°C	Time/min	Conv (%)	Sel (%)	TON[a]	Reference
1.0 wt.% Pt_1/h-NC SAC	40	10	97.1	77.8	31,157	This work*
1.0 wt.% nano-Pt/h-NC	40	10	93.8	47.1	2,018	This work*
Pure h-NCs	40	60	0	0	0	This work*
0.25 wt.% Pt/XC-72	40	10	9.7	41.3	1,225	This work*
Pure XC-72	40	60	0	0	0	This work*
0.08 wt.% Pt_1/FeO_x	40	50	96.5	98.6	1,493	Wei et al., 2014
0.2 wt.% Pt/TiO_2	40	390		93.1	56	Serna et al., 2009
0.01 wt.% Pt/TiO_2	85	360		48.4	1,449	Serna et al., 2009
1.4 wt.% Pt/ZnO	75	/		97	1,560	Berguerand et al., 2015
Commercial Pt/C[b]	75	/	/	0	0	Berguerand et al., 2015

Table 1. Chemoselective Hydrogenation of 3-Nitrostyrene on Pt/h-NC Catalysts Compared with Most Active Catalysts Reported in the Literature

[a]The amount of the produced 3-vinylaniline molecules per active site per hour. The turnover number (TON) value was measured by keeping the substrate conversion below 25% by tuning the molecular ratio of Pt atoms to 3-nitrostyrene molecules.

*Reaction conditions: H_2 pressure = 5 bar; Pt/substrate = 0.078%; 8 mL reaction mixture: 0.5 mmol 3-nitrostyrene, ethanol as solvent, O-xylene as internal standard.

[b]The Pt loading of the commercial Pt/C catalyst is 1.0 wt.% (Berguerand et al., 2015).

For the used 1.0 wt.% Pt_1/h-NC SAC, most of the single Pt atoms (~99%) were still isolated and only very few small aggregates of loosely connected Pt atoms (~0.4 nm) were detected (Figure S8). These atomically dispersed aggregates do not seem to form Pt-Pt bond since the distances among these Pt atoms are much larger than that of crystalline Pt clusters (Yang et al., 2015). The fact that the Pt single atoms remained isolated after the catalytic reaction suggests that the isolated single Pt atoms were strongly anchored onto the edge/defect sites of the h-NCs. Moreover, atomic resolution HAADF-STEM images show that the individual Pt atoms primarily decorated the edges/steps of nanoscale pieces of graphene sheets (indicated by the green dash lines in Figures 1D and S4) present in the h-NCs. These edge carbon atoms strongly interact with the individual single Pt atoms as suggested by density functional theory (DFT) calculations (Wei et al., 2017a). Since the XC-72 carbon support is highly graphitic and does not possess many strong anchoring edge/defect sites, the originally atomically dispersed Pt atoms in the XC-72 carbon sintered into Pt nanoparticles/clusters with an average size of 1.1 $\pm$ 0.1 nm after one cycle of selective hydrogenation of 3-nitrostyrene (Figure S9). These results suggest that, although the Pt was atomically dispersed in the fresh Pt/XC-72 catalyst, these Pt atoms did not strongly interact with the XC-72 carbon and thus sintered during the hydrogenation reaction. The XC-72 carbon and the h-NCs are structurally very different, resulting in different degrees of Pt-carbon interactions and consequently the differences in catalytic performance.

Characterization of the Edge Site Defects in the Fabricated Pt1/h-NC SACs

To understand why the synthesized h-NCs strongly anchored Pt single atoms, Raman spectroscopy, capable of providing the density of defects of carbon materials (Ferrari and Robertson, 2000; Sadezky et al., 2005), was used to evaluate the properties of the carbon supports. By using the empirical formula models (Cançado et al., 2006; Tuinstra and Koenig, 1970), the defect density of h-NCs was estimated to be about five times higher than that of the XC-72 carbon (Figure S10 and Table S1), which suggests that the synthesized h-NCs consist of numerous defects (edge sites) as evidenced in STEM images. After Pt single atoms were deposited on the h-NCs, the defect density decreased by ~17% (Table S1). Based on the STEM images (Figures 1D and S8) as well as the spectroscopy data we propose that the drop of the estimated defect density by Raman spectroscopy is caused by the strong anchoring of Pt atoms to the edge/defect sites of the nanoscale graphene sheets. DFT calculations suggested that single Pt atoms can directly bond with graphene edges with a binding energy as high as 7.46 eV (Wei et al., 2017a). After Pt single atoms were deposited on the XC-72 carbon, the defect density slightly decreased by ~6%, suggesting that the XC-72 carbon cannot strongly anchor the atomically dispersed Pt atoms, which

corroborates the STEM results that the atomically dispersed Pt atoms sintered to particles (~1.1 nm) after the hydrogenation reaction.

The Electronic Structure of the Fabricated Pt_1/h-NC SACs

The X-ray photoelectron spectroscopy (XPS) C1s spectrum of the 1.0 wt.% Pt_1/h-NC SAC shows that, in addition to the carbon sp^2 (284.7 eV) and sp^3 (285.2 eV) peaks, there is a new component located at 284.3 eV (Figure S11A), assignable to a Pt-C bond originating from a strong covalent interaction between Pt atoms and the under-coordinated carbon atoms of the h-NCs (Rajasekaran et al., 2012; Ng et al., 2010). XPS spectra (Figure 2) suggest that the 1.0 wt.% Pt_1/h-NC SAC contains only ~10% of Pt^{2+} species, whereas ~90% of the Pt species possess a binding energy of 71.8 eV, higher than that of the metallic Pt species (71.3 eV) but lower than that of the Pt^{2+} species (72.6 eV). We denote these Pt species as $Pt^{\delta+}$ ($0<\delta<2$). The occurrence of the $Pt^{\delta+}$ (71.8 eV) species can be attributed to the formation of Pt-C bonds with electron transfer from the Pt single atoms to the carbon support (Alderucci et al., 1995; Axnanda et al., 2015). The presence of the Pt^{2+} species may result from the oxidation by the oxygen-containing groups present on the surfaces of the h-NCs as evidenced by the O 1s spectrum (Figure S11B), which shows three components assignable to the Pt-OH (532.1 eV, 60%), Pt-H_2O (533.1 eV, 37%), and Pt-O species (530.0 eV, 3%) (Alderucci et al., 1995). The STEM images, Raman spectra, and XPS data all support the conclusion that the Pt single atoms decorated the edges of the cross-linked nanoscale graphene sheets in the h-NCs (Figures 1D and S4) and directly bonded with the edge carbon atoms to form strong Pt-C bonds (Rajasekaran et al., 2012; Ng et al., 2010), probably arising from the hybridization of Pt 5d and the abundant C 2p orbitals of the edge carbon atoms (Tang et al., 2011).

The Pt 4f XPS spectrum of the 1.0 wt.% nano-Pt/h-NC (Figure 2) exhibits mostly metallic Pt species (71.3 eV, 61%), an appreciable amount of Pt^{2+} (72.6 eV, 30%) and a minor amount of $Pt^{\delta+}$ (71.8 eV, 9%). The XPS C1s spectrum of the 1.0 wt.% nano-Pt/h-NC (Figure S11A) shows that, in addition to the carbon sp^2 (284.7 eV) and sp^3 (285.2 eV) peaks, there is also a very weak peak at 284.3 eV, suggesting the formation of a minor amount of Pt-C bond, which may originate from the interaction of the edge atoms of the Pt nanoparticles with the carbon support (Rajasekaran et al., 2012; Ng et al., 2010). The Pt 4f XPS spectrum of the 0.25 wt.% Pt_1/XC-72 catalyst could not be quantitatively analyzed because of the signal-to-noise problem (Yang et al.,

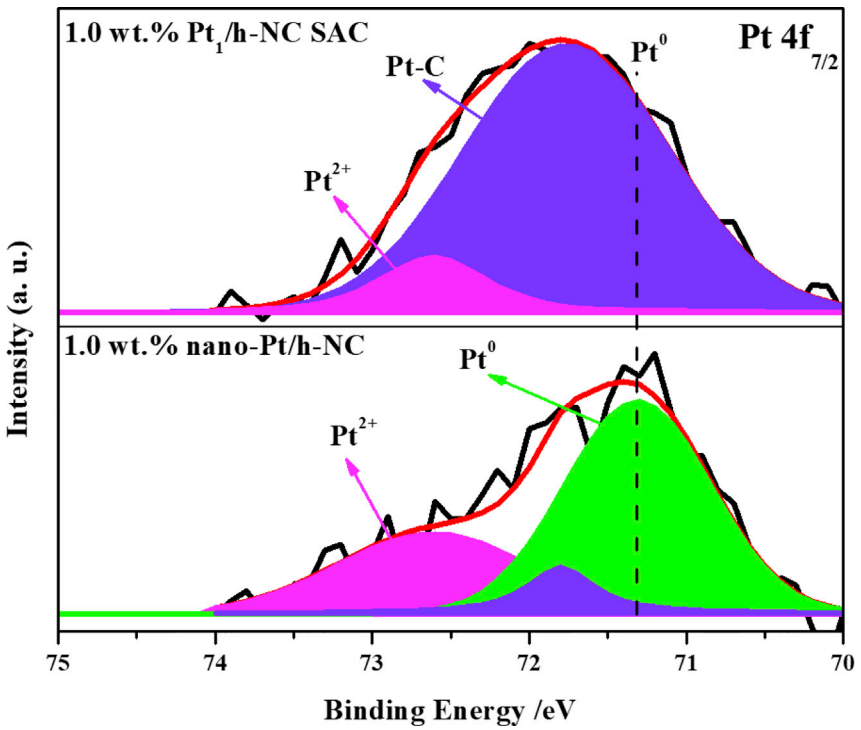

Figure 2. Electronic Structures of h-NCs and h-NC Supported Pt Catalysts
Pt 4f 7/2 XPS of 1.0 wt.% Pt_1/h-NC SAC and 1.0 wt.% nano-Pt/h-NC.

2015; Zhang et al., 2016). But the oxidation state of the atomically dispersed Pt atoms in the 0.25 wt.% Pt_1/XC-72 catalyst seems to be between +2 and +4 (Figure S12), suggesting that the Pt species may primarily be in the form of highly dispersed Pt oxides. The absence of an obvious Pt-C peak (Figure S13) in the 0.25 wt.% Pt_1/XC-72 suggests that the atomically dispersed Pt atoms did not interact strongly with the graphitic carbon support, resulting in sinter of Pt atoms and small clusters during the hydrogenation reaction, corroborating the conclusion from the STEM imaging observation (Figure S9) and Raman spectroscopy data (Figure S10).

Effects of Strong Pt-Carbon Interaction on Catalytic Performance

The geometric and electronic properties of active metal species play a crucial role in determining the adsorption behavior of functional groups and the dissociation behavior of H_2 (Armbrüster et al., 2012; Blaser et al., 2009; Wei et al., 2014, 2017b; Lou et al., 2018). Pt metals show excellent catalytic capability of H_2 dissociation with a reaction barrier as low as 0 and 0.067 eV on Pt (001) and Pt (111) surfaces, respectively (Pasteur et al., 1997; Olsen et al., 1999). The strength of the Pt-H bonds is too high (even close to H-H in H_2) to be efficient and chemoselective for catalytic reactions (Ludwig et al., 2006; Corma et al., 2008). For selective hydrogenation to targeted products, a catalyst that possesses facile activation of H_2 and weak adsorption strength of the dissociated H atoms can exhibit optimal efficiency in balancing activity and selectivity for the targeted product (Lucci et al., 2015a, 2015b, 2016; Kyriakou et al., 2012). For the Pt_1/h-NC SAC system, the metal-carbon interaction results in electron transfer from the Pt atoms to the carbon support and they most probably maintain their valence state under the hydrogenation reaction conditions. The electron depletion of the edge-carbon-anchored Pt atoms induces downshift of the d-band center of the $Pt^{\delta+}$ species ($0< \delta < 2$) and consequently reduces, when compared with the metallic Pt species, the binding strength of the dissociatively adsorbed hydrogen atoms (Armbrüster et al., 2012; Namba et al., 2018). Such a change of the d-band center of the single Pt species facilitates the activation of H_2 and thus provides more activated and weakly bound hydrogen species to accelerate the catalytic reaction. Under hydrogenation reaction conditions, the nanometer-sized Pt oxide species can be easily reduced to the metallic state and sintered to Pt particles (Huizinga et al., 1984; Duan et al., 2018), which will strongly bind the adsorbed H species, resulting in the lack of weakly bound hydrogen species for catalytic reactions. Furthermore, the H_2 dissociation over Pt_1/h-NCs may follow the heterolytic dissociation procedure to yield $H^{\delta+}$ and $H^{\delta-}$ species on the Pt-carbon interface, which may significantly enhance the catalytic activity of hydrogenation reactions as reported in the literature (Liu et al., 2016; Wang et al., 2016; Dhiman and Polshettiwar, 2018). The spillover effects of the activated H species over the carbon support cannot be ruled out. The influence of such spillover H species on the observed activity and selectivity on hydrogenation reactions is not clear and needs to be further investigated. Based on our characterization and catalytic testing data, we propose that the strong Pt-carbon interaction in the Pt_1/h-NCs significantly modifies the electronic structure of the carbon-edge-anchored single Pt atoms and correspondingly their catalytic properties for H_2 activation. The enhanced electronic SMSI makes the 1.0 wt.% Pt_1/h-NC SAC a much more highly active catalyst than that of the atomically dispersed 0.25 wt.% Pt_1/XC-72 and 1.0 wt.% nano-Pt/h-NC catalysts for 3-nitrostyrene hydrogenation.

DISCUSSION

The selective hydrogenation of the C=C bonds is considered to be highly sensitive to the size of the Pt ensembles (Wei et al., 2014; Corma et al., 2008; Lucci et al., 2015a, 2015b). On the other hand, the selectivity for nitro groups is independent of the size of the Pt particles (Corma et al., 2008; Peng et al., 2018). It has been reported that Pt single atoms especially prefer the adsorption of nitro groups to the C=C groups (Wei et al., 2014; Peng et al., 2018). The dissociated H species may spillover via carbon support to the nitro groups that are activated by single Pt atoms to complete the catalytic reaction cycle (Wei et al., 2014). Hence, the strong Pt_1-C interaction in the 1.0 wt.% Pt_1/h-NC SAC not only enhances H_2 activation to provide more activated and weakly bound hydrogen species but also provides stable single sites that inhibit the C=C activation and simultaneously enhances the nitro group activation. The strong electronic Pt-carbon interaction not only enhances anchoring of single Pt atoms to the edge carbon atoms of the h-NCs but also significantly modifies their catalytic properties for selective hydrogenation. As a result of the strong Pt_1-carbon interaction the Pt atoms transfer electrons to carbon support to form $Pt^{\delta+}$ species, which are proposed to be the active sites for facilely dissociating H_2 and preferential adsorption of the specific sites of the reactant molecules. The fabricated Pt_1/h-NC SACs exhibited excellent catalytic performance for selective hydrogenation of 3-nitrostyrene to 3-vinylaniline because of the covalent bonding of Pt_1 to the edge carbon atoms of the nanoscale graphene pieces in the synthesized h-NCs.

Although further improvement in designing the carbon structure to tune the Pt-carbon interaction may result in further improved selectivity, our research work clearly demonstrated the power in utilizing the electronic SMSI in SACs to significantly enhance the activity for desired reaction products. The strategy utilized in this work is general and can be broadened to construct different catalytic systems, especially SACs, for a plethora of catalytic reactions, including liquid- and gas-phase transformation of important molecules.

Limitations of Study

Our research on electronic strong metal-carbon interaction in SACs has extended the SMSI concept to broader catalyst systems for tuning catalytic properties of strongly anchored single metal atoms. A combined density functional theory and Monte Carlo approach for quantifying the metal-carbon interactions at the reaction temperatures can provide an in-depth understanding on the electronic strong metal-carbon interaction in SACs and may provide guidance for designing better catalysts for liquid-phase transformation of important molecules. The reaction mechanisms of selective 3-nitrostyrene hydrogenation, the spillover effects of the activated H species, and the role of the highly defective carbon structures in the adsorption of reactant molecules need to be further investigated. Although the study of these important questions on the fundamental understanding of selective hydrogenation of important complex molecules is beyond the scope of this current work, such fundamental studies can provide guidance on effectively utilizing the strong metal-carbon interaction to design robust SACs with desired catalytic performance.

METHODS

All methods can be found in the accompanying Transparent Methods supplemental file.

SUPPLEMENTAL INFORMATION

Supplemental Information can be found online at https://doi.org/10.1016/j.isci.2019.02.016.

ACKNOWLEDGMENTS

The authors acknowledge funding by the National Science Foundation under CHE-1465057 and the use of facilities within the Eyring Materials Center and the John M. Cowley Center for High Resolution Electron Microscopy at Arizona State University.

AUTHOR CONTRIBUTIONS

J.L. designed and conceived the experiments, acquired the STEM images and analyzed the experimental data, and reviewed and edited this manuscript. Y.L. designed, synthesized, and tested the catalysts; conducted the spectroscopy experiments; and analyzed the data and drafted the manuscript. H.W. synthesized the hollow nanocarbons.

DECLARATION OF INTERESTS

The authors declare no competing interests.

Received: November 27, 2018
Revised: January 20, 2019
Accepted: February 14, 2019
Published: March 29, 2019

REFERENCES

Alderucci, V., Pino, L., Antonucci, P.L., Roh, W., Cho, J., Kim, H., Cocke, D.L., and Antonucci, V. (1995). XPS study of surface oxidation of carbon-supported Pt catalysts. Mater. Chem. Phys. *41*, 9–14.

Armbrüster, M., Behrens, M., Cinquini, F., Föttinger, K., Grin, Y., Haghofer, A., Klötzer, B., Knop-Gericke, A., Lorenz, H., Ota, A., et al. (2012). How to control the selectivity of palladium-based catalysts in hydrogenation reactions: the role of subsurface chemistry. ChemCatChem *4*, 1048–1063.

Axnanda, S., Crumlin, E.J., Mao, B., Rani, S., Chang, R., Karlsson, P.G., Edwards, M.O., Lundqvist, M., Moberg, R., Ross, P., et al. (2015). Using "tender" X-ray ambient pressure X-ray photoelectron spectroscopy as a direct probe of solid-liquid interface. Sci. Rep. *5*, 9788.

Berguerand, C., Yarulin, A., Cárdenas-Lizana, F., Wärnå, J., Sulman, E., Murzin, D.Y., and Kiwi-Minsker, L. (2015). Chemoselective liquid phase hydrogenation of 3-nitrostyrene over Pt nanoparticles: synergy with ZnO support. Ind. Eng. Chem. Res. *54*, 8659–8669.

Blaser, H.U., Steiner, H., and Studer, M. (2009). Selective catalytic hydrogenation of functionalized nitroarenes: an update. ChemCatChem *1*, 210–221.

Bonanni, S., Ait-Mansour, K., Harbich, W., and Brune, H. (2012). Effect of the TiO_2 reduction state on the catalytic CO oxidation on deposited size-selected Pt clusters. J. Am. Chem. Soc. *134*, 3445–3450.

Cançado, L.G., Takai, K., Enoki, T., Endo, M., Kim, Y.A., Mizusaki, H., Jorio, A., Coelho, L.N.,

Magalhães-Paniago, R., and Pimenta, M.A. (2006). General equation for the determination of the crystallite size La of nanographite by Raman spectroscopy. Appl. Phys. Lett. *88*, 163106.

Charlier, J.C. (2002). Defects in carbon nanotubes. Acc. Chem. Res. *35*, 1063–1069.

Chen, Y., Ji, S., Chen, C., Peng, Q., Wang, D., and Li, Y. (2018). Single-atom catalysts: synthetic strategies and electrochemical applications. Joule *2*, 1242–1264.

Corma, A., and Serna, P. (2006). Chemoselective hydrogenation of nitro compounds with supported gold catalysts. Science *313*, 332–334.

Corma, A., Serna, P., Concepcion, P., and Calvino, J.J. (2008). Transforming nonselective into chemoselective metal catalysts for the hydrogenation of substituted nitroaromatics. J. Am. Chem. Soc. *130*, 8748–8753.

Cui, X., Li, H., Wang, Y., Hu, Y., Hua, L., Li, H., Han, X., Liu, Q., Yang, F., He, L., et al. (2018). Room-temperature methane conversion by graphene-confined single iron atoms. Chem *4*, 1902–1910.

Dhiman, M., and Polshettiwar, V. (2018). Supported single atom and pseudo-single atom of metals as sustainable heterogeneous nanocatalysts. ChemCatChem *10*, 881–906.

Dong, J., Fu, Q., Jiang, Z., Mei, B., and Bao, X. (2018). Carbide-supported Au catalysts for water-gas shift reactions: a new territory for the strong metal-support interaction effect. J. Am. Chem. Soc. *140*, 13808–13816.

Downing, R.S., Kunkeler, P.J., and vanBekkum, H. (1997). Catalytic syntheses of aromatic amines. Catal. Today *37*, 121–136.

Duan, S., Wang, R., and Liu, J. (2018). Stability investigation of a high number density Pt_1/Fe_2O_3 single-atom catalyst under different gas environments by HAADF-STEM. Nanotechnology *29*, 204002.

Ebbesen, T.W., and Takada, T. (1995). Topological and SP^3 defect structures in nanotubes. Carbon *33*, 973–978.

Fei, H., Dong, J., Arellano-Jimenez, M.J., Ye, G., Dong Kim, N., Samuel, E.L., Peng, Z., Zhu, Z., Qin, F., Bao, J., et al. (2015). Atomic cobalt on nitrogen-doped graphene for hydrogen generation. Nat. Commun. *6*, 8668.

Ferrari, A.C., and Robertson, J. (2000). Interpretation of Raman spectra of disordered and amorphous carbon. Phys. Rev. B *61*, 14095–14107.

Gates, B.C., Flytzani-Stephanopoulos, M., Dixon, D.A., and Katz, A. (2017). Atomically dispersed supported metal catalysts: perspectives and suggestions for future research. Catal. Sci. Technol. *7*, 4259–4275.

Huizinga, T., Van Grondelle, J., and Prins, R. (1984). A temperature programmed reduction study of Pt on Al_2O_3 and TiO_2. Appl. Catal. *10*, 199–213.

Kyriakou, G., Boucher, M.B., Jewell, A.D., Lewis, E.A., Lawton, T.J., Baber, A.E., Tierney, H.L., Flytzani-Stephanopoulos, M., and Sykes, E.C.H. (2012). Isolated metal atom geometries as a strategy for selective heterogeneous hydrogenations. Science *335*, 1209–1212.

Lee, J., Burt, S.P., Carrero, C.A., Alba-Rubio, A.C., Ro, I., O'Neill, B.J., Kim, H.J., Jackson, D.H.K., Kuech, T.F., Hermans, I., et al. (2015). Stabilizing cobalt catalysts for aqueous-phase reactions by strong metal-support interaction. J. Catal. *330*, 19–27.

Li, Q., Chen, W., Xiao, H., Gong, Y., Li, Z., Zheng, L., Zheng, X., Yan, W., Cheong, W.C., Shen, R., et al. (2018). Fe isolated single atoms on S, N codoped carbon by copolymer pyrolysis strategy for highly efficient oxygen reduction reaction. Adv. Mater. *30*, 1800588.

Liu, H., Peng, X., and Liu, X. (2018). Single-atom catalysts for the hydrogen evolution reaction. ChemElectroChem. *5*, 2963–2974.

Liu, J. (2017a). Aberration-corrected scanning transmission electron microscopy in single-atom catalysis: probing the catalytically active centers. Chin. J. Catal. *38*, 1460–1472.

Liu, J.Y. (2017b). Catalysis by supported single metal atoms. ACS Catal. *7*, 34–59.

Liu, P.X., Zhao, Y., Qin, R.X., Mo, S.G., Chen, G.X., Gu, L., Chevrier, D.M., Zhang, P., Guo, Q., Zang, D.D., et al. (2016). Photochemical route for synthesizing atomically dispersed palladium catalysts. Science *352*, 797–801.

Liu, X., Liu, M.H., Luo, Y.C., Mou, C.Y., Lin, S.D., Cheng, H., Chen, J.M., Lee, J.F., and Lin, T.S. (2012). Strong metal-support interactions between gold nanoparticles and ZnO nanorods in CO oxidation. J. Am. Chem. Soc. *134*, 10251–10258.

Lordi, V., Yao, N., and Wei, J. (2001). Method for supporting platinum on single-walled carbon nanotubes for a selective hydrogenation catalyst. Chem. Mater. *13*, 733–737.

Lou, Y., Xu, J., Wu, H., and Liu, J. (2018). Hollow carbon anchored highly dispersed Pd species for selective hydrogenation of 3-nitrostyrene: metal-carbon interaction. Chem. Commun. *54*, 13248–13251.

Lucci, F.R., Darby, M.T., Mattera, M.F., Ivimey, C.J., Therrien, A.J., Michaelides, A., Stamatakis, M., and Sykes, E.C. (2016). Controlling hydrogen activation, spillover, and desorption with Pd-Au single-atom alloys. J. Phys. Chem. Lett. *7*, 480–485.

Lucci, F.R., Liu, J., Marcinkowski, M.D., Yang, M., Allard, L.F., Flytzani-Stephanopoulos, M., and Sykes, E.C. (2015a). Selective hydrogenation of 1,3-butadiene on platinum-copper alloys at the single-atom limit. Nat. Commun. *6*, 8550.

Lucci, F.R., Marcinkowski, M.D., Lawton, T.J., and Sykes, E.C.H. (2015b). H_2 activation and spillover on catalytically relevant Pt–Cu single atom alloys. J. Phys. Chem. C *119*, 24351–24357.

Ludwig, J., Vlachos, D.G., van Duin, A.C., and Goddard, W.A. (2006). Dynamics of the dissociation of hydrogen on stepped platinum surfaces using the ReaxFF reactive force field. J. Phys. Chem. B *110*, 4274–4282.

Matsubu, J.C., Zhang, S., DeRita, L., Marinkovic, N.S., Chen, J.G., Graham, G.W., Pan, X., and Christopher, P. (2017). Adsorbate-mediated strong metal-support interactions in oxide-supported Rh catalysts. Nat. Chem. *9*, 120–127.

Namba, K., Ogura, S., Ohno, S., Di, W., Kato, K., Wilde, M., Pletikosic, I., Pervan, P., Milun, M., and Fukutani, K. (2018). Acceleration of hydrogen absorption by palladium through surface alloying with gold. Proc. Natl. Acad. Sci. U S A *115*, 7896–7900.

Ng, M.L., Balog, R., Hornekær, L., Preobrajenski, A.B., Vinogradov, N.A., Mårtensson, N., and Schulte, K. (2010). Controlling hydrogenation of graphene on transition metals. J. Phys. Chem. C *114*, 18559–18565.

Olsen, R.A., Kroes, G.J., and Baerends, E.J. (1999). Atomic and molecular hydrogen interacting with Pt (111). J. Chem. Phys. *111*, 11155–11163.

Pasteur, A.T., Dixon-Warren, S.J., Ge, Q., and King, D.A. (1997). Dynamics of hydrogen dissociation on Pt: steering, screening and thermal roughening effects. J. Chem. Phys. *106*, 8896–8904.

Peng, Y., Geng, Z., Zhao, S., Wang, L., Li, H., Wang, X., Zheng, X., Zhu, J., Li, Z., Si, R., and Zeng, J. (2018). Pt single atoms embedded in the surface of Ni nanocrystals as highly active catalysts for selective hydrogenation of nitro compounds. Nano Lett. *18*, 3785–3791.

Qiao, B., Liu, J., Wang, Y.G., Lin, Q., Liu, X., Wang, A., Li, J., Zhang, T., and Liu, J. (2015). Highly efficient catalysis of preferential oxidation of CO in H_2-rich stream by gold single-atom catalysts. ACS Catal. *5*, 6249–6254.

Qiao, B., Wang, A., Yang, X., Allard, L.F., Jiang, Z., Cui, Y., Liu, J., Li, J., and Zhang, T. (2011). Single-atom catalysis of CO oxidation using Pt_1/FeO_x. Nat. Chem. *3*, 634–641.

Rajasekaran, S., Kaya, S., Abild-Pedersen, F., Anniyev, T., Yang, F., Stacchiola, D., Ogasawara, H., and Nilsson, A. (2012). Reversible graphene-metal contact through hydrogenation. Phys. Rev. B *86*, 075417.

Sadezky, A., Muckenhuber, H., Grothe, H., Niessner, R., and Pöschl, U. (2005). Raman microspectroscopy of soot and related carbonaceous materials: spectral analysis and structural information. Carbon *43*, 1731–1742.

Serna, P., Concepción, P., and Corma, A. (2009). Design of highly active and chemoselective bimetallic gold–platinum hydrogenation catalysts through kinetic and isotopic studies. J. Catal. *265*, 19–25.

Sonstrom, P., Arndt, D., Wang, X., Zielasek, V., and Baumer, M. (2011). Ligand capping of colloidally synthesized nanoparticles-a way to tune metal-support interactions in heterogeneous gas-phase catalysis. Angew. Chem. Int. Ed. *50*, 3888–3891.

Su, D.S., Wen, G., Wu, S., Peng, F., and Schlogl, R. (2017). Carbocatalysis in liquid-phase reactions. Angew. Chem. Int. Ed. *56*, 936–964.

Tang, H., Liu, F., Wei, J., Qiao, B., Zhao, K., Su, Y., Jin, C., Li, L., Liu, J.J., Wang, J., and Zhang, T. (2016a). Ultrastable hydroxyapatite/titanium-dioxide-supported gold nanocatalyst with strong

metal-support interaction for carbon monoxide oxidation. Angew. Chem. Int. Ed. *55*, 10606–10611.

Tang, H., Wei, J., Liu, F., Qiao, B., Pan, X., Li, L., Liu, J., Wang, J., and Zhang, T. (2016b). Strong metal-support interactions between gold nanoparticles and nonoxides. J. Am. Chem. Soc. *138*, 56–59.

Tang, Y., Yang, Z., and Dai, X. (2011). Trapping of metal atoms in the defects on graphene. J. Chem. Phys. *135*, 224704.

Tauster, S.J., Fung, S.C., and Garten, R.L. (1978). Strong metal-support interactions. Group 8 noble metals supported on titanium dioxide. J. Am. Chem. Soc. *100*, 170–175.

Tuinstra, F., and Koenig, J.L. (1970). Characterization of graphite fiber surfaces with Raman spectroscopy. J. Comp. Mater. *4*, 492–499.

Vannice, M. (1979). Metal-support effects on the activity and selectivity of Ni catalysts in CO/H_2 synthesis reactions. J. Catal. *56*, 236–248.

Wang, A., Li, J., and Zhang, T. (2018). Heterogeneous single-atom catalysis. Nat. Rev. Chem. *2*, 65–81.

Wang, J., Zhao, X., Lei, N., Li, L., Zhang, L., Xu, S., Miao, S., Pan, X., Wang, A., and Zhang, T. (2016). Hydrogenolysis of glycerol to 1, 3-propanediol under low hydrogen pressure over WO_x-supported single/pseudo-single atom Pt catalyst. ChemSusChem *9*, 784–790.

Wang, L., Zhang, J., Zhu, Y., Xu, S., Wang, C., Bian, C., Meng, X., and Xiao, F.S. (2017). Strong metal–support interactions achieved by hydroxide-to-oxide support transformation for preparation of sinter-resistant gold nanoparticle catalysts. ACS Catal. *7*, 7461–7465.

Wei, H., Huang, K., Wang, D., Zhang, R., Ge, B., Ma, J., Wen, B., Zhang, S., Li, Q., Lei, M., et al. (2017a). Iced photochemical reduction to synthesize atomically dispersed metals by suppressing nanocrystal growth. Nat. Commun. *8*, 1490.

Wei, H., Liu, X., Wang, A., Zhang, L., Qiao, B., Yang, X., Huang, Y., Miao, S., Liu, J., and Zhang, T. (2014). FeO_x-supported platinum single-atom and pseudo-single-atom catalysts for chemoselective hydrogenation of functionalized nitroarenes. Nat. Commun. *5*, 5634.

Wei, H., Ren, Y., Wang, A., Liu, X., Liu, X., Zhang, L., Miao, S., Li, L., Liu, J., Wang, J., et al. (2017b). Remarkable effect of alkalis on the chemoselective hydrogenation of functionalized nitroarenes over high-loading Pt/FeO_x catalysts. Chem. Sci. *8*, 5126–5131.

Yan, H., Cheng, H., Yi, H., Lin, Y., Yao, T., Wang, C., Li, J., Wei, S., and Lu, J. (2015). Single-atom Pd_1/graphene catalyst achieved by atomic layer deposition: remarkable performance in selective hydrogenation of 1,3-butadiene. J. Am. Chem. Soc. *137*, 10484–10487.

Yang, M., Liu, J., Lee, S., Zugic, B., Huang, J., Allard, L.F., and Flytzani-Stephanopoulos, M. (2015). A common single-site $Pt(II)$-$O(OH)_x$-species stabilized by sodium on "active" and "inert" supports catalyzes the water-gas shift reaction. J. Am. Chem. Soc. *137*, 3470–3473.

Zhang, B., Asakura, H., Zhang, J., Zhang, J., De, S., and Yan, N. (2016). Stabilizing a platinum single-atom catalyst on supported phosphomolybdic acid without compromising hydrogenation activity. Angew. Chem. Int. Ed. *55*, 8319–8323.

Zitolo, A., Goellner, V., Armel, V., Sougrati, M.T., Mineva, T., Stievano, L., Fonda, E., and Jaouen, F. (2015). Identification of catalytic sites for oxygen reduction in iron- and nitrogen-doped graphene materials. Nat. Mater. *14*, 937–942.

ISCI, Volume *13*

Supplemental Information

Nanocarbon-Edge-Anchored High-Density Pt Atoms for 3-nitrostyrene Hydrogenation: Strong Metal-Carbon Interaction

Yang Lou, Honglu Wu, and Jingyue Liu

SUPPLEMENTAL INFORMATION

Nanocarbon-Edge-Anchored High-Density Single Pt Atoms for Selective Hydrogenation of 3-nitrostyrene: Strong Metal-Carbon Interaction

Yang Lou[1], Honglu Wu[1], Jingyue Liu[1, 2]*

[1]Department of Physics, Arizona State University, Tempe, Arizona 85287, United States

[2]Lead contact

*Correspondence: jingyue.liu@asu.edu

Contents:

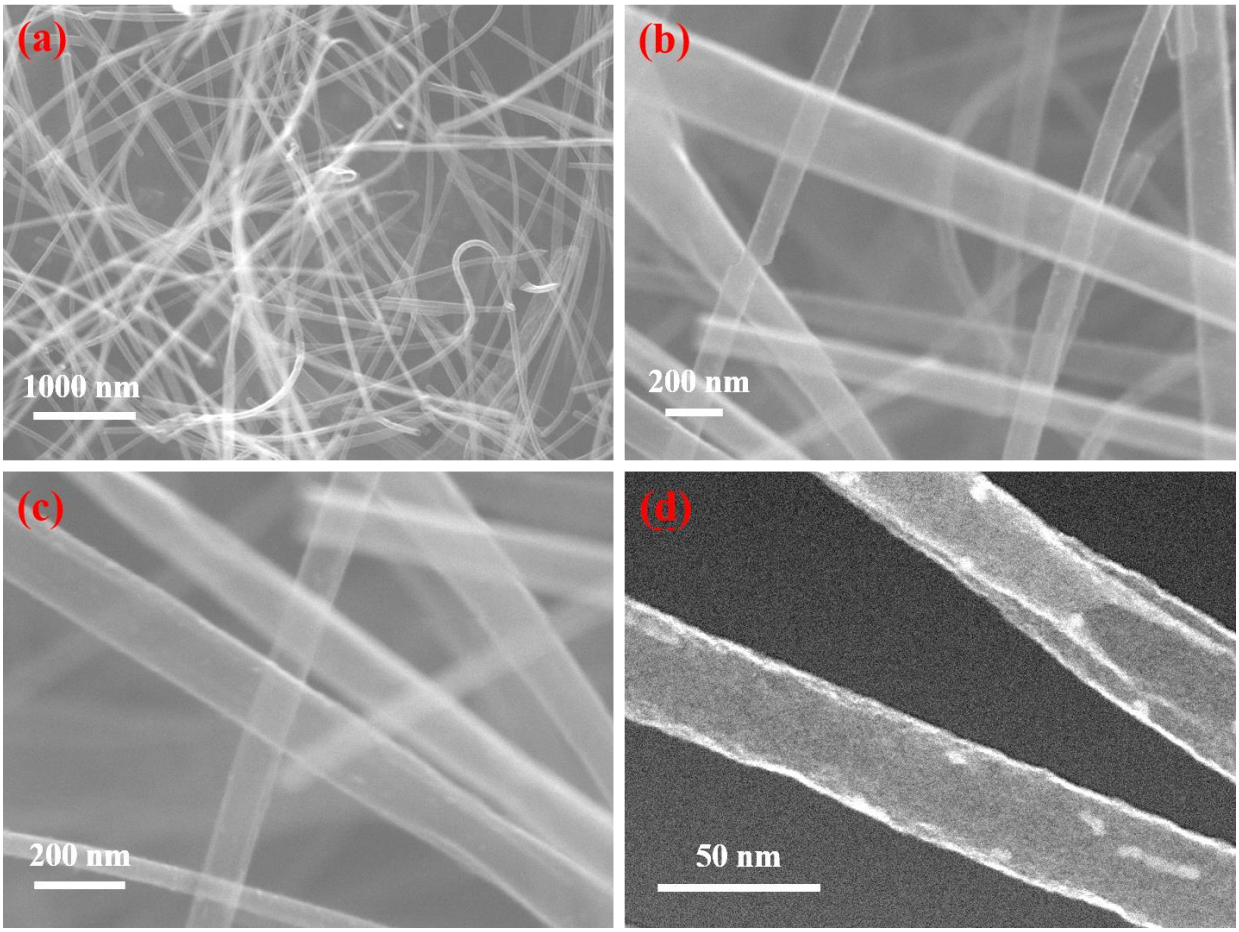

Figure S1 SEM images (a-c) and aberration-corrected HAADF-STEM image (d) of h-NCs show the general morphology and the wall thicknesses of the synthesized hollow nanocarbon tubes, Related to Figure 1.

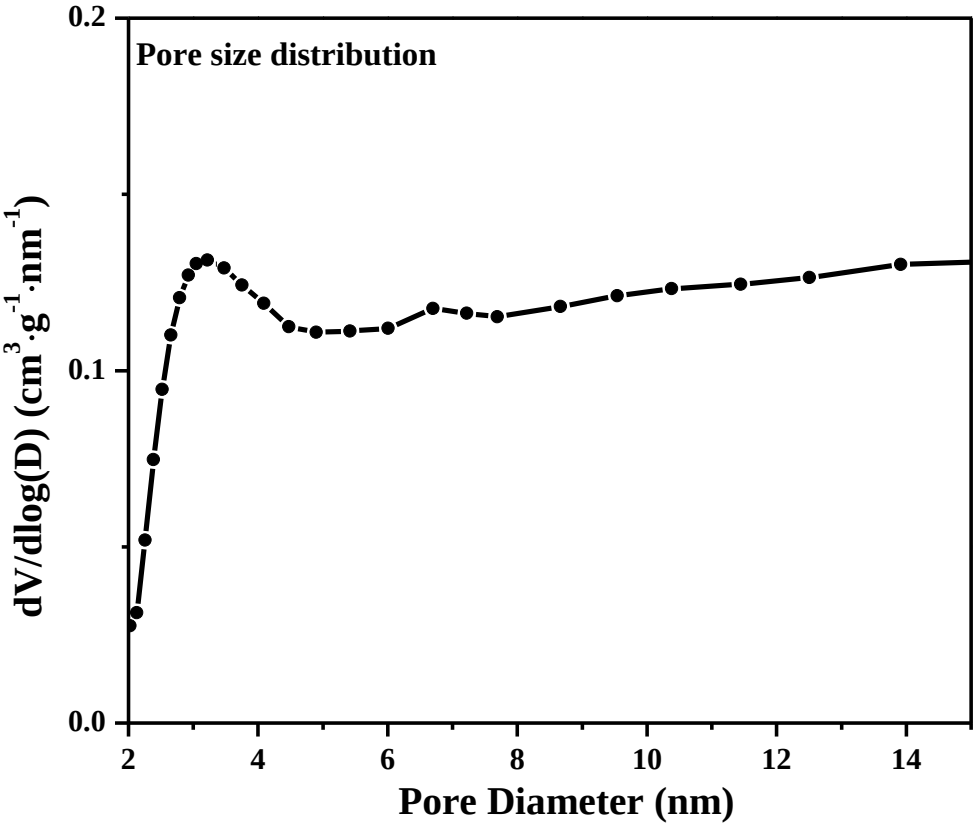

Figure S2 Pore size distribution of the synthesized h-NCs, Related to Figure 1.

The average size of the pores on the wall of the h-NCs was estimated to be 3.2 nm.

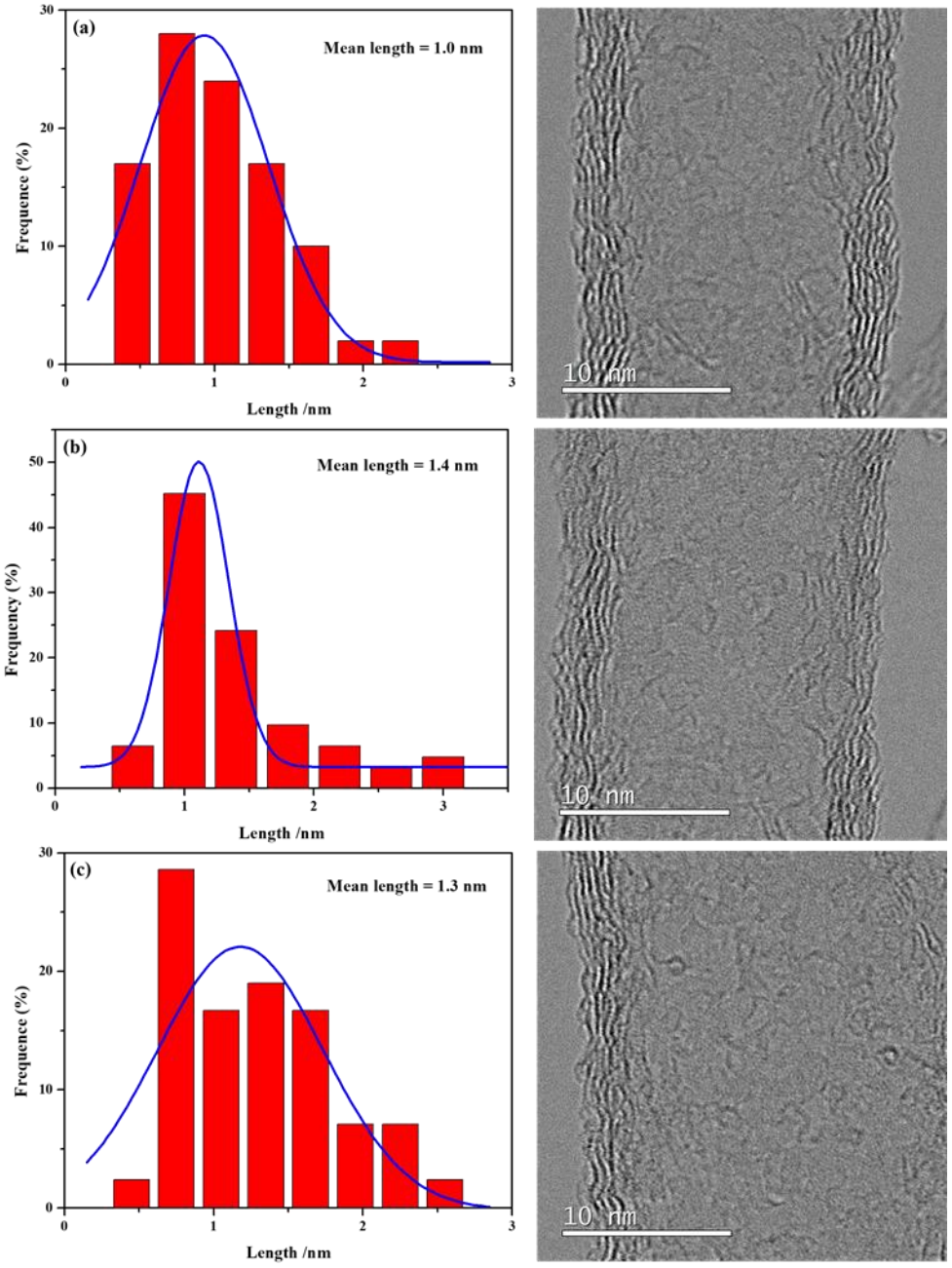

Figure S3 Aberration-corrected STEM images of h-NCs and the size distributions of the corresponding nanoscale graphene sheets (a-c), Related to Figure 1.

The synthesized h-NCs are composed of stacking of hyper-cross-linked graphene sheets, resulting in highly disordered structure, high surface area and tube-type morphology. The hyper-cross-linked graphene sheets exhibit high number density edge sites (Figure S3a-S3c). The lateral sizes of the graphene sheets range from 0.5 nm to 3.1 nm with an average length of 1.2 ± 0.2 nm. The histograms were obtained by measuring the identifiable lengths of the graphene sheets in the corresponding bright-field STEM images.

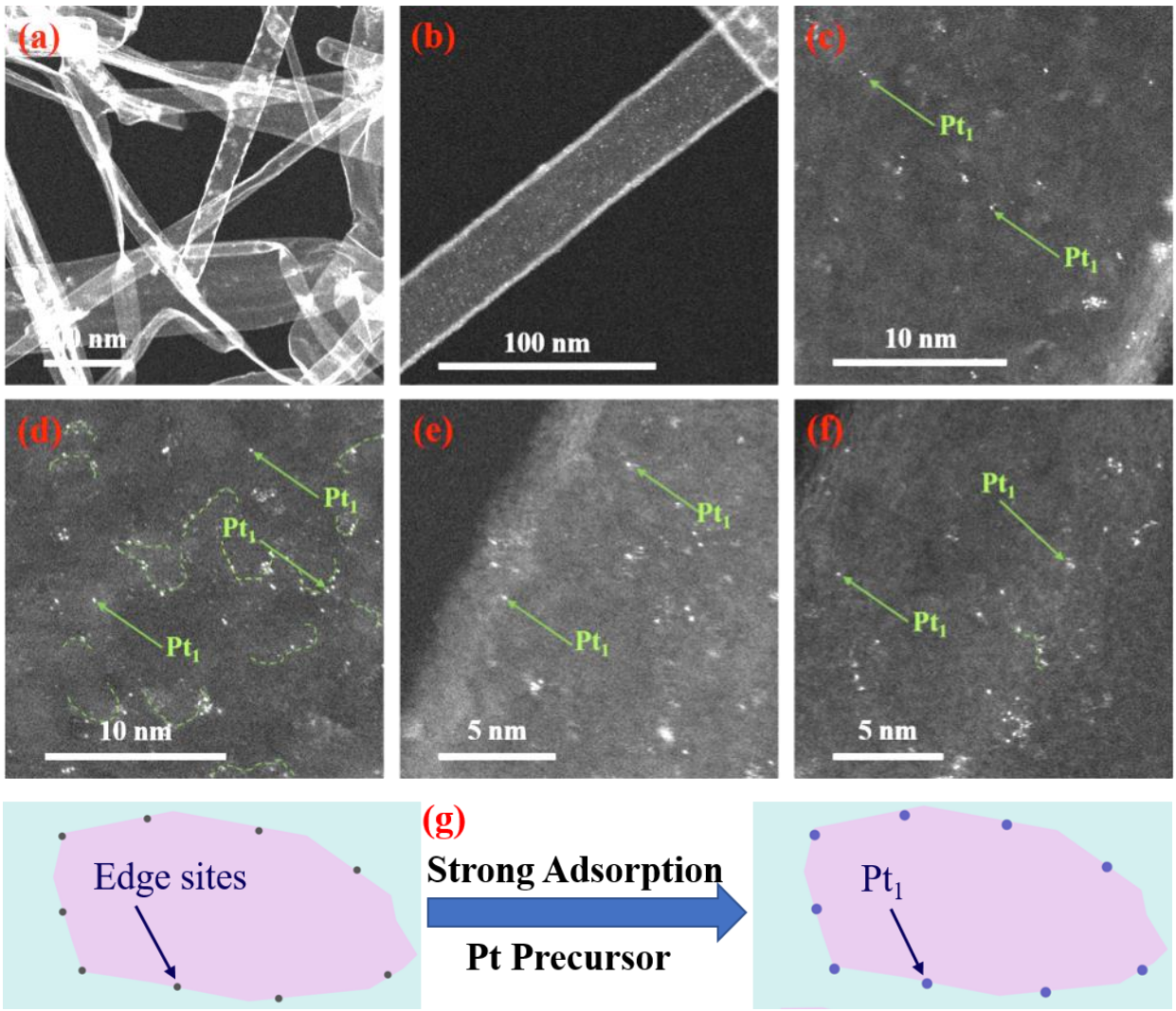

Figure S4 Low-magnification and high-magnification aberration-corrected HAADF/STEM images of fresh 1.0 wt.% Pt_1/h-NC SAC (a-f); schematic diagram for single Pt atoms anchored on the edges of graphene sheets of h-NCs (g), Related to Figure 1.

As clearly shown in Figure S4 (a), low-magnification HAADF-STEM image confirms the absence of any Pt particles or clusters in the fresh 1.0 wt.% Pt_1/h-NC SAC. The high-magnification HAADF-STEM images (Figure S4 (b-f)) confirm that the Pt atoms are atomically dispersed on the surfaces of the h-HC support. By examining numerous low/high magnification HAADF-STEM images (Figure S4 (a-f)) obtained from different regions of the synthesized h-NCs, we unambiguously concluded that the fresh1.0 wt.% Pt_1/h-NC SAC contains only isolated Pt atoms without the presence of any Pt particles or clusters. Moreover, Pt atoms are mainly decorated on the edges of those hyper-cross-linked graphene sheets. A small amount of single Pt atoms may have trapped between the layers of the graphene sheets (Yan et al., 2015; Tang et al., 2016). However, since the sizes of the graphene sheets are so small and there are almost no observable close stacking of parallel graphene sheets in the synthesized h-NCs the Pt atoms should not be stably trapped between layers of graphene. Figure S4 (g) is the schematic diagram to illustrate the anchoring of single Pt atoms onto the edges of nanoscale graphene sheets in the synthesized h-NCs.

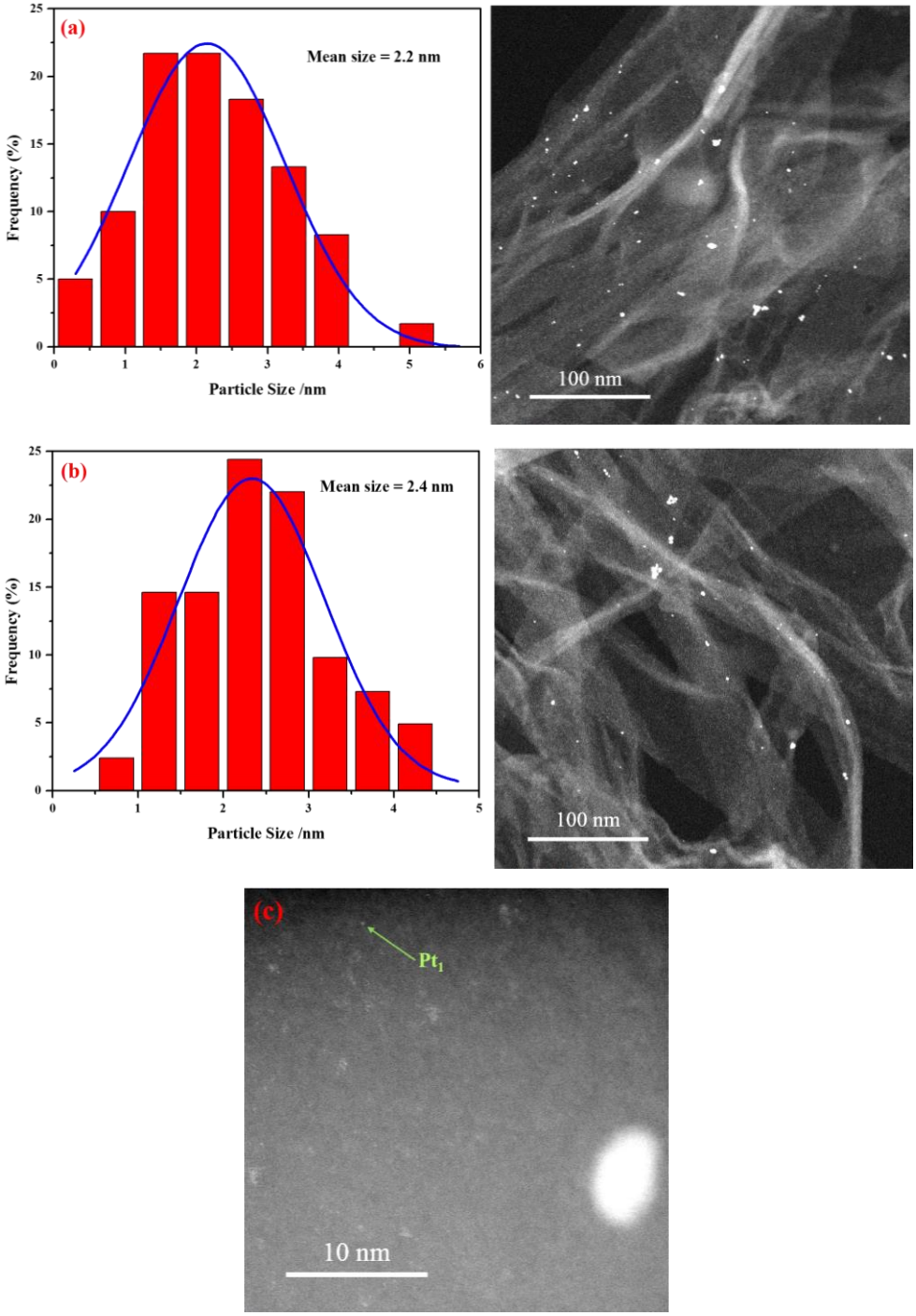

Figure S5 Low-magnification and high-magnification aberration-corrected HAADF/STEM images of 1.0 wt.% nano-Pt/h-NC, Related to Figure 1. The average particle size is 2.3 ± 0.1 nm.

Pt particles of 1.0 wt.% nano-Pt/h-NCs are distributed on the surfaces of the h-NCs (Figure S5 a-b) and the average size of the Pt particles was measured to be 2.3 ± 0.1 nm. From the high-magnification image (c), we can see the presence of some single Pt atoms in the 1.0 wt.% nano-Pt/h-NC catalyst. The presence of these anchored Pt single atoms may make appreciable contribution to the experimentally measured activity and selectivity for 3-nitrostyrene hydrogenation over the 1.0 wt.% nano-Pt/h-NC catalyst.

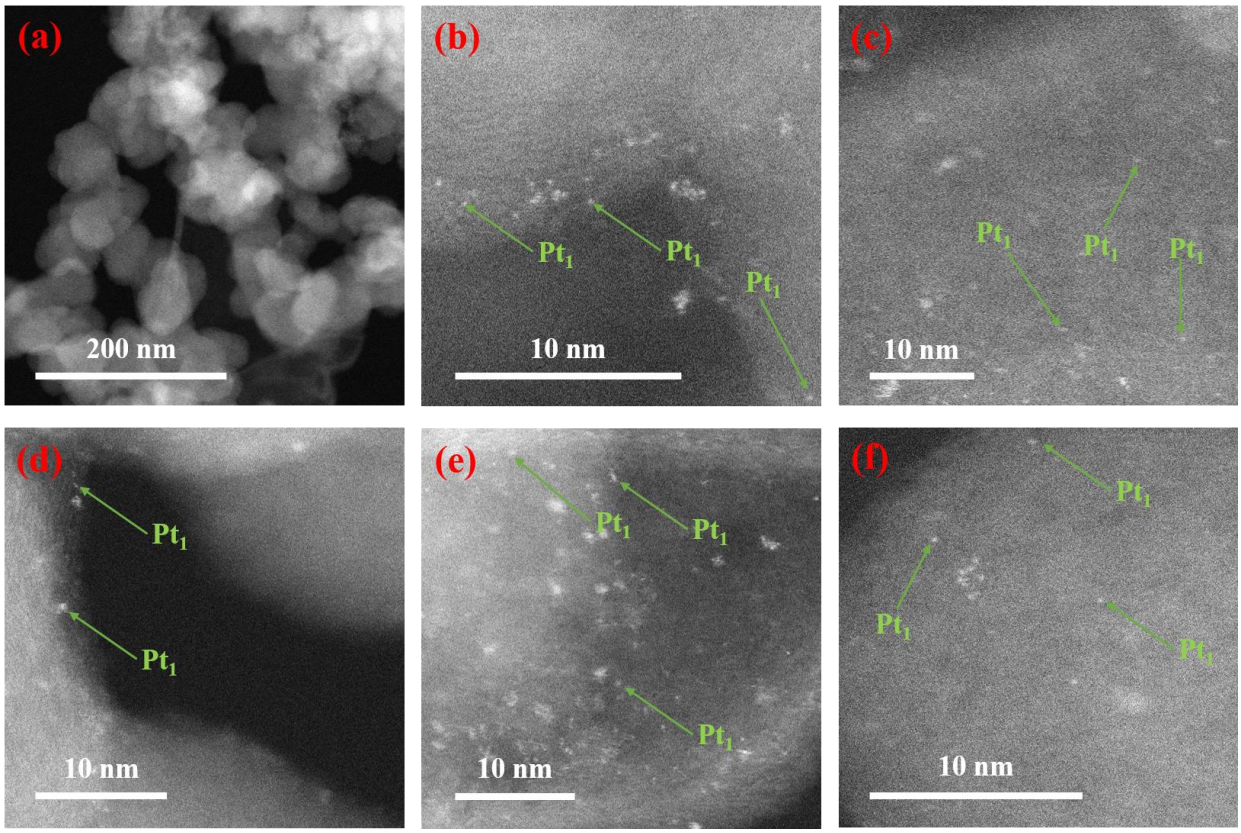

Figure S6 Low-magnification and high-magnification aberration-corrected HAADF/STEM images of an as-synthesized atomically dispersed 0.25 wt.% Pt_1/XC-72 catalyst, Related to Figure 1.

Figure S6 (a) and numerous other low-magnification HAADF-STEM images confirm the absence of any Pt particles or clusters in the fresh 0.25 wt.% Pt_1/XC-72 catalyst. The high-magnification HAADF-STEM images (Figure S6 (b-f)) confirm that the Pt atoms are atomically dispersed on the surfaces of the XC-72 support. By examining numerous low/high magnification HAADF-STEM images (Figure S6 (a-f)) obtained from different regions, we unambiguously concluded that the as-prepared 0.25 wt.% Pt_1/XC-72 contains only isolated Pt atoms and atomically dispersed small Pt clusters of a few Pt atoms without the presence of Pt particles.

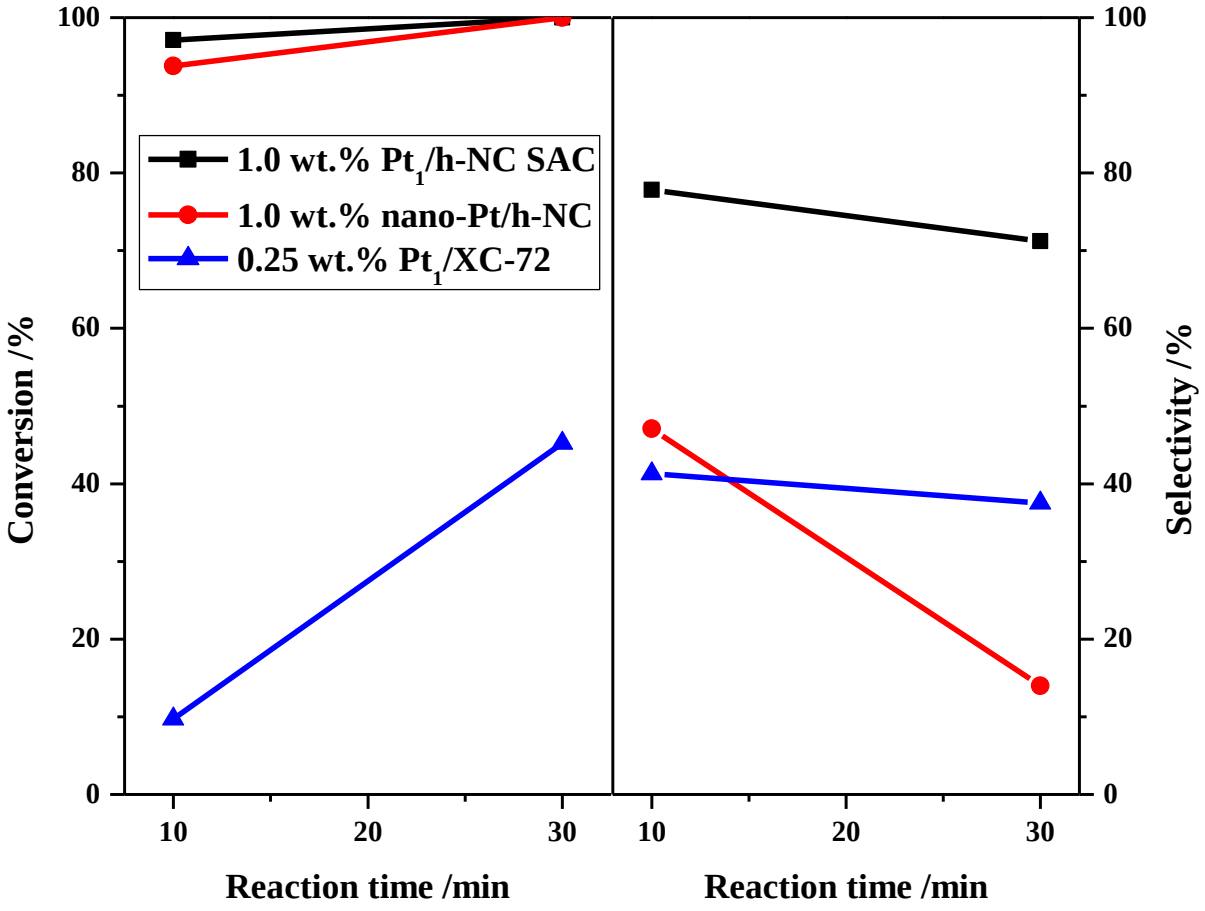

Figure S7 Time-dependent conversion and selectivity of 1.0 wt.% Pt_1/h-NC SAC, 1.0 wt.% nano-Pt/h-NC and 0.25 wt.% Pt_1/XC-72 for selective hydrogenation of 3-nitrostyrene, Related to Table 1.

With the increase of reaction time, the catalytic conversion of 3-nitrostyrene over 1.0 wt.% Pt_1/h-NC SAC, 1.0 wt.% nano-Pt/h-NC and 0.25 wt.% Pt_1/XC-72 gradually increases but the selectivity toward the 3-vinylaniline gradually decreases. Further hydrogenation of the produced 3-vinylaniline to 3-ethylaniline is possible but the formation of small Pt clusters or particles with reaction time also decreases the selectivity toward 3-vinylaniline. Promoters to either boost the activity or selectivity may need to be developed to increase the yield of the final product.

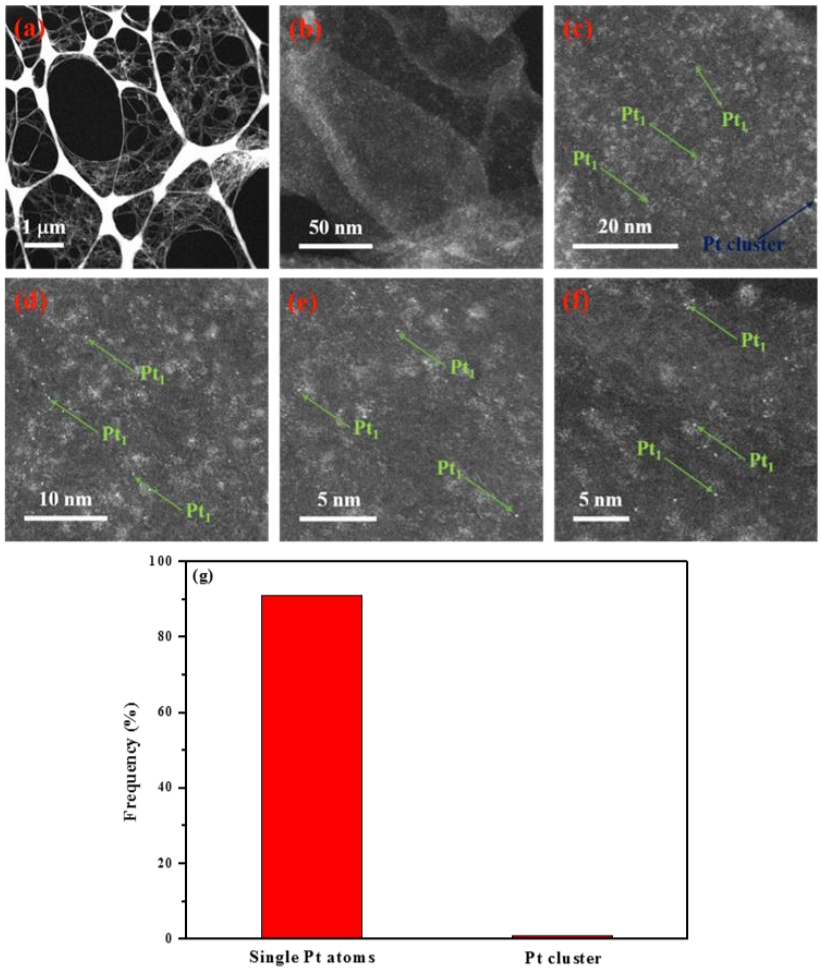

Figure S8 Low-magnification and high-magnification aberration-corrected HAADF/STEM images of used 1.0 wt.% Pt_1/h-NC SAC, Related to Figure 1. The 1.0 wt.% Pt_1/h-NC SAC was used for 30 min at a reaction temperature of 40 °C.

As clearly shown in Figure S8 (a-b), low-magnification HAADF-STEM images did not show Pt particles in the used 1.0 wt.% Pt_1/h-NC SAC. Only the presence of very few Pt clusters (around 0.4-0.5 nm) are observable (Figure S8 b). The high-magnification HAADF-STEM images (Figure S8 (c-f)) confirm that the used catalyst consists primarily of isolated single Pt atoms uniformly dispersed on the surfaces of the h-NCs.

In order to quantify the amount of the small Pt clusters present in the used 1.0 wt.% Pt_1/h-NC SAC, we conducted a statistical analysis of the number of Pt single atoms and small clusters (Figure S8 c) and the result is shown in Figure S8 g. We estimated that ~99% of the Pt in the used 1.0 wt.% Pt_1/h-NC SAC remained as isolated single Pt atoms after the hydrogenation reaction. Only ~1% of the Pt single atoms in the fresh catalyst sintered to atomically dispersed, loosely connected Pt clusters without the formation of Pt-Pt bonding (Yang et al., 2015). These results suggest that all the Pt atoms were still atomically dispersed after the catalytic hydrogenation reaction. Such stable SACs assure that the measured catalytic activity and kinetic data originated from the anchored single Pt atoms rather than from Pt clusters/particles.

By examining numerous low/high magnification HAADF-STEM images (Figure S8 (a-f)) obtained from different regions, we unambiguously concluded that the used 1.0 wt.% Pt_1/h-NC SAC still predominately consists of isolated Pt atoms (99%). However, after three cycles, many of the Pt atoms aggregated to form Pt clusters.

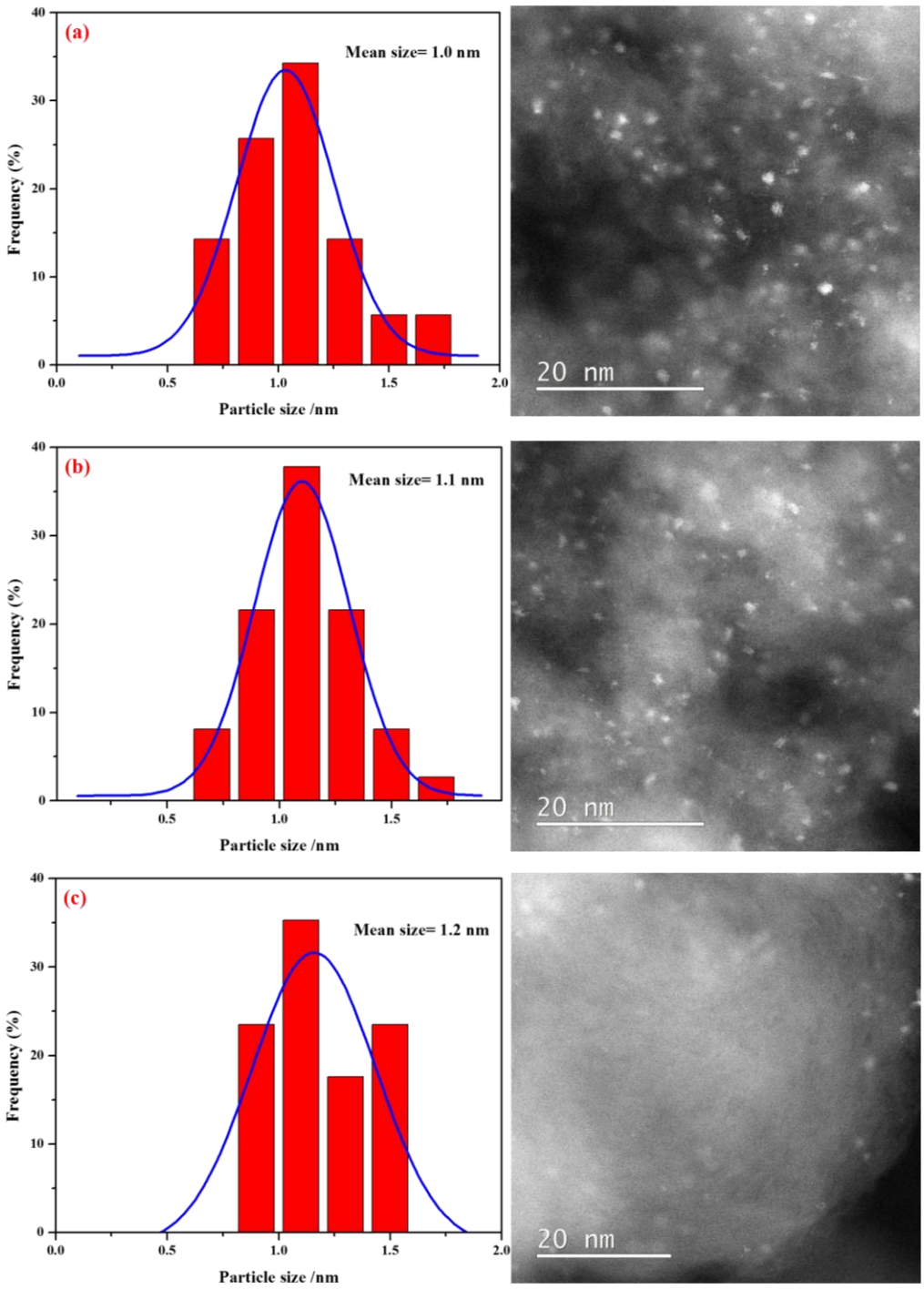

Figure S9 Pt particle size distributions and HAADF/STEM images of the used 0.25 wt.% Pt_1/XC-72, Related to Figure 1. The 0.25 wt.% Pt_1/XC-72 was used for 30 min at a reaction temperature of 40 ^oC.

As clearly shown in Figure S9 (a-c), the HAADF-STEM images confirm the sintering of the atomically dispersed 0.25 wt.% Pt_1/XC-72 into Pt clusters/particles during the hydrogenation reaction. The sintered Pt particles are uniformly distributed on the surfaces of the XC-72 carbon powders. Statistical analyses of the sintered Pt particles of the used 0.25 wt.% Pt_1/XC-72 catalyst yielded an average size of 1.1 ± 0.1 nm.

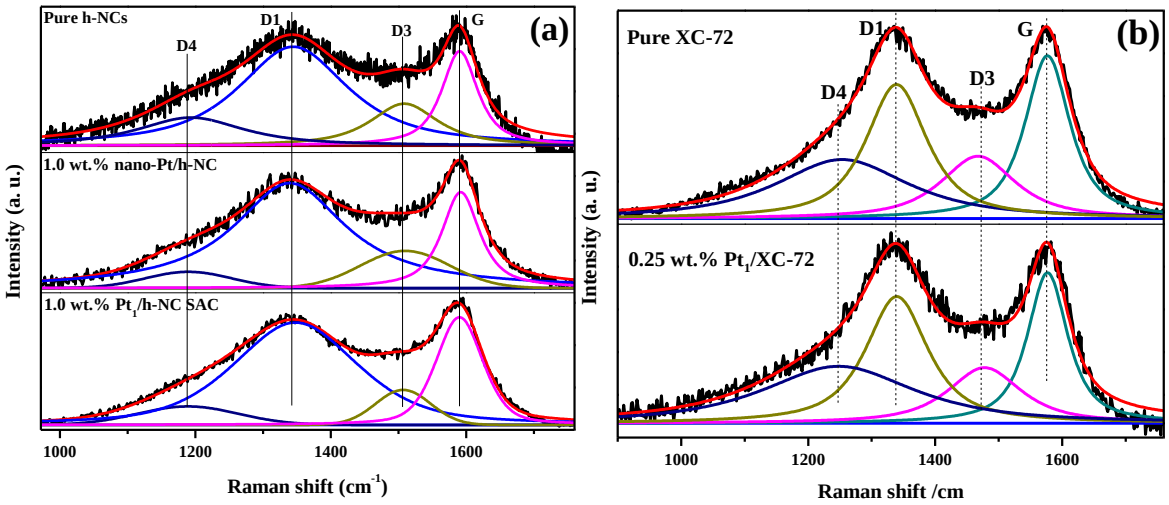

Figure S10 Raman spectra of carbon and carbon supported Pt catalysts, Related to Figure 2. Pure h-NCs, 1.0 wt.% nano-Pt/h-NC and 1.0 wt.% Pt_1/h-NC SAC (a); Pure XC-72 and 0.25 wt.% Pt_1/ XC-72 (b).

Raman spectroscopy, capable of providing useful information on the density of defects of carbon materials based on the ratio of D1 to G band intensities (I_{D1}/I_G) (Ferrari et al., 2000; Sadezky et al., 2005), was used to evaluate the carbon supports. As shown in Figure S10 (a-b), the peaks at 1190 cm^{-1}, 1345 cm^{-1}, and 1508 cm^{-1} can be assigned to the D4, D1 and D3 band and the peak at 1591 cm^{-1} can be assigned to the G band (Gopinadhan et al., 2013; Chernyak et al., 2017). The D_1-band is associated with the defects within the carbon atom plane and the G-band originates from the sp^2-bonded carbon atoms (Wang et al., 2016). The presence of the D3 band can be attributed to the presence of stacking faults, changes in the interlayer spacing, and the mixed breathing and asymmetric stretching vibrational modes of sp^2-carbons near defects (Maldonado et al., 2006; Smith et al., 2016). The broad component of D4 can be assigned to amorphous impurities in graphite materials (Prawer et al., 2000). The ratio between D1 and G band intensities (I_{D1}/I_G) can be used to quantify the degree of disorder and the presence of sp^3-hybridized carbon atoms within the structure. The pure h-NCs support exhibits a high I_{D1}/I_G ratio (1.1), suggesting the presence of high-density defects in the synthesized h-NCs (Wang et al., 2016; Wen et al., 2015). The ratio between D1 and G band intensities (I_{D1}/I_G) of pure XC-72 is 0.85, which is in line with the previously reported data (0.84) (Peng et al., 2017). The ratio between D1 and G band intensities (I_{D1}/I_G) of the 0.25 wt.% Pt_1/XC-72 is ~0.84.

The I_{D1}/I_G values for the h-NCs and XC-72 carbon are calculated to be 1.1 and 0.85 respectively, suggesting high density of edge/defect sites present in the h-NCs (Sadezky et al., 2005). From analyses of atomic resolution STEM images and Raman spectra we can confidently conclude that the synthesized h-NCs consist of numerous nanoscale graphene sheets with large number of edge sites. Prior to characterizing the carbon defects in the control carbon supports the pure carbon powders were pretreated/exposed to the identical condition that was used for synthesizing Pt single atom catalysts. Therefore, the effect of the chemical processes of adding the Pt single atoms onto the carbon supports on the Raman spectroscopy measurement was significantly minimized.

The experimentally measured I_{D1}/I_G ratio of the 1.0 wt.% Pt_1/h-NC SAC decreased from 1.1 to 0.9. We propose that the drop in the I_{D1}/I_G ratio is caused by the strong anchoring of Pt atoms to the edge/defect sites of graphene sheets, which are evidenced in the STEM images (Figure 1d and S8). For the XC-72 carbon, the I_{D1}/I_G ratio slightly decreased by ~1%, suggesting that the atomically dispersed Pt atoms were not strongly affect the XC-72 carbon, which corroborates STEM results that Pt atoms sintered to particles (~ 1.1 nm) after the hydrogenation reaction. Since the density of the Pt particles in the 1.0 wt.% nano-Pt/h-NC is extremely low, the I_{D1}/I_G ratio of 1.0 wt.% nano-Pt/h-NC is only decreased by 2%.

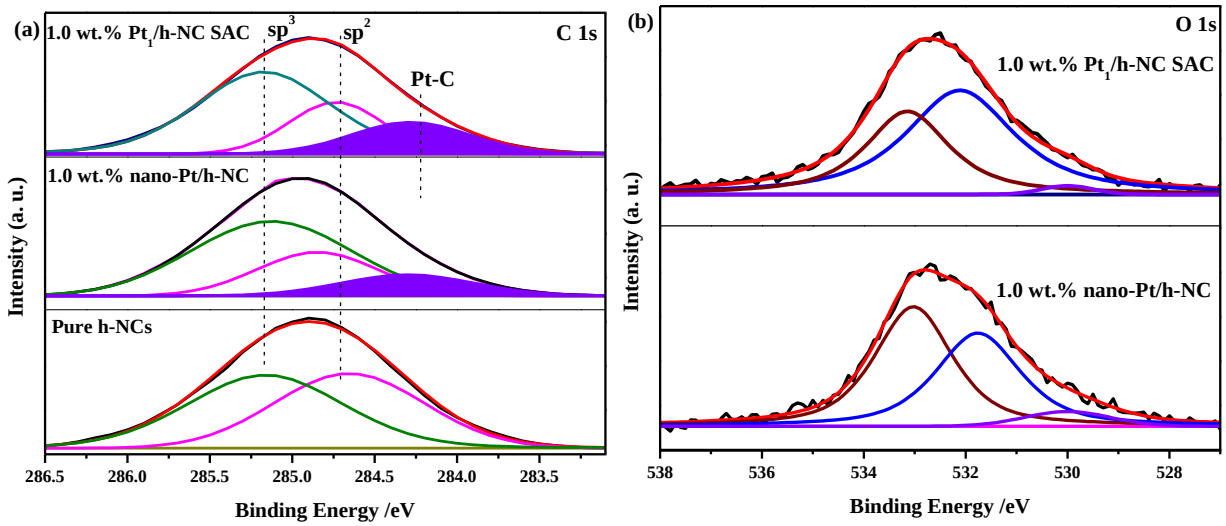

Figure S11 X-ray Photoelectron Spectroscopy of h-NCs and h-NC supported Pt catalysts: C 1s spectra (a) and O 1s (b), Related to Figure 2.

XPS spectra of the fresh 1.0 wt.% nano-Pt/h-NC catalyst and the pure h-NCs show only the carbon sp^2 (284.7 eV) and sp^3 (285.2 eV) peaks. However, the XPS spectrum, obtained from the 1.0 wt.% Pt_1/h-NC SAC, shows, in addition to the carbon sp^2 (284.7 eV) and sp^3 (285.2 eV) peaks, a new component located at 284.3 eV, assignable to a Pt-C bond originating from strong covalent interaction between Pt atoms and under-coordinated carbon atoms of the h-NCs (Rajasekaran et al., 2012; Ng et al., 2010). Our XPS data suggest that charge transfer occurred between the anchored Pt atoms and the edge carbon atoms in the h-NC mesoporous carbon. Such charge transfer results in oxidized Pt atoms, $Pt^{\delta+}$ ($0< \delta <2$), which can have catalytic properties different from those of the zero valent Pt^0. Similarly, the XPS C1s spectrum of the 1.0 wt.% nano-Pt/h-NC shows that in addition to the carbon sp^2 (284.7 eV) and sp^3 (285.2 eV) peaks, there is also a weak peak at 284.3 eV, probably originating from the presence of a small amount of Pt-C bond in the 1.0 wt.% nano-Pt/h-NC catalyst.

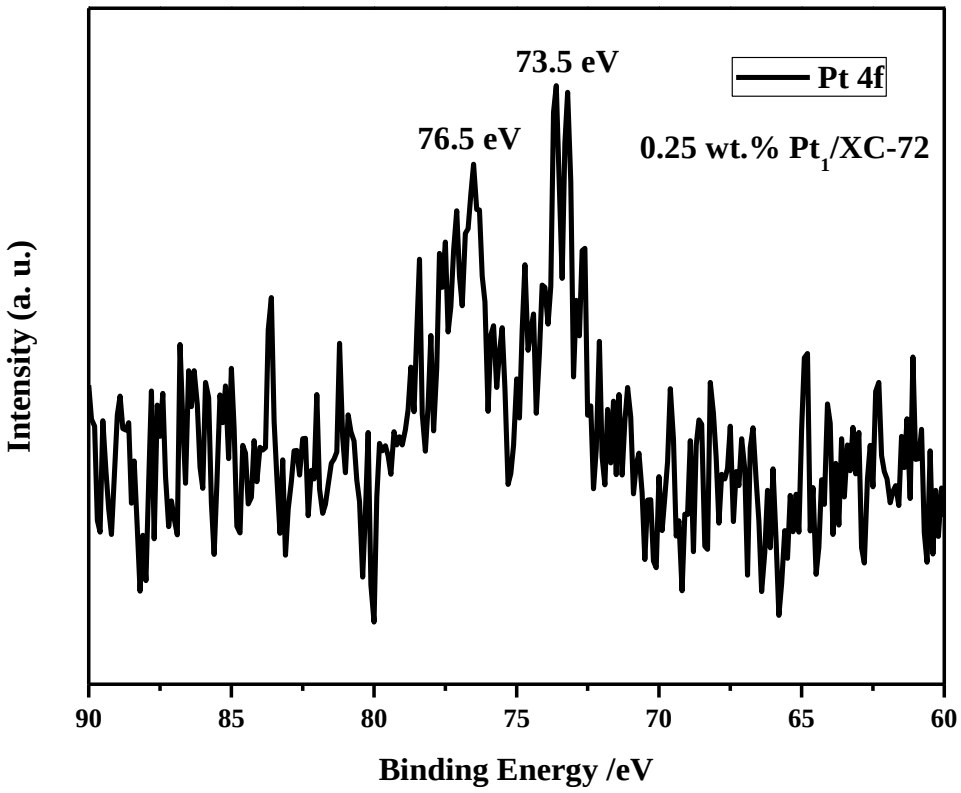

Figure S12 XPS Pt 4f spectrum of atomically dispersed 0.25 wt.% Pt_1/XC-72, Related to Figure 2.

The Pt 4f XPS spectrum of the 0.25 wt.% Pt_1/XC-72 catalyst could not be quantitatively analyzed due to the signal-to-noise problem (Ref 32 and 43). But the obvious peak located in the range of 73.2 and 73.5 eV as shown in Figure S12 indicates the oxidation state of Pt atoms in 0.25 wt.% Pt_1/XC-72 catalyst should be between +2 (72.6 eV) (Alderucci et al., 1995; Axnanda et al., 2015) and +4 (74.1 eV) (Peuckert et al., 1984; Ono et al., 2010).

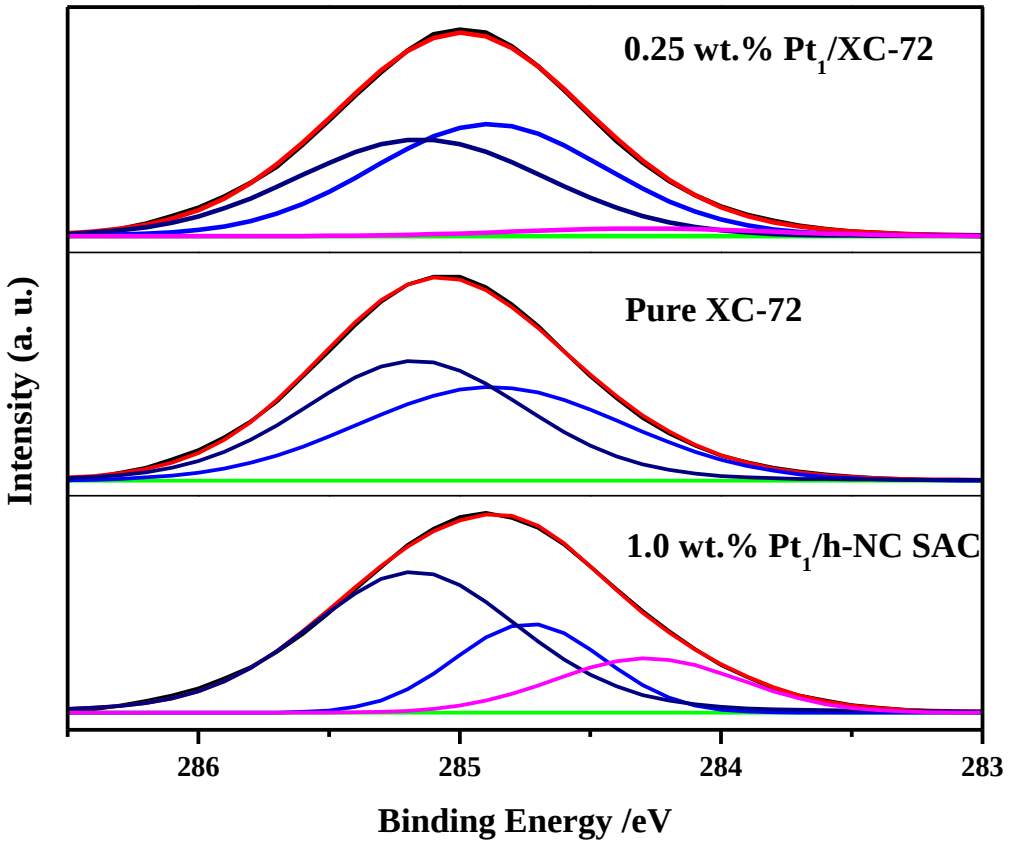

Figure S13 XPS C 1s spectra of: 1.0 wt.% Pt_1/h-NC SAC, atomically dispersed 0.25 wt.% Pt_1/XC-72 and pure XC-72, Related to Figure 2.

The C 1s XPS spectrum of the 0.25 wt.% Pt_1/XC-72 is similar to that of the pure XC-72 carbon, mainly displaying sp^2 (284.7 eV) and sp^3 (285.2 eV) components as shown in Figure S13. The absence of an obvious Pt-C peak in the 0.25 wt.% Pt_1/XC-72 suggests that the interaction of the atomically dispersed Pt atoms with the graphitic carbon support is much weaker than that between the Pt single atoms and the h-NCs in the 1.0 wt.% nano-Pt/h-NC SAC.

Table S1 Summary of the defect density and crystallite size of the synthesized Pt SACs and nano-Pt catalysts, Related to Table 1.

Sample	La /nm[a]	Defect density[b]	Defect density[c]
h-NCs	6.6 (1.2[d])	2.27E+12 (6.94E+13[e])	7.21E+11 (2.21E+13[e])
1.0 wt.% Pt_1/h-NC SAC	7.2	1.92E+12	6.11E+11
1.0 wt.% nano-Pt/h-NC	6.7	2.21E+12	7.04E+11
XC-72	14.2 (2.6[d])	4.96E+11 (1.48E+13[e])	1.58E+11 (4.71E+12[e])
1.0 wt.% Pt/XC-72	14.6	4.66E+11	1.48E+11

a: The crystallite size (La) is estimated based on the La (nm)=560*($El^{\wedge 4}$)*$(I_D/I_G)^{-1}$, El is the excitation energy laser energy used in the Raman experiment in eV units and the integrated intensities (peak areas) of the D and G bands instead of the ratio of peak amplitudes is used (Cançado et al., 2006). And the estimated value is normally larger than that of actual one (Chen et al., 2009).

b: The defect density (n_a/cm^{-2}) is calculated by the formula of $n_a=(1/La)^2$ (Cançado et al., 2006).

c: The defect density (n_a/cm^{-2}) is calculated by the formula of $n_a=10^{14}/\pi La^2$ (Zhong et al., 2014; Cancado et al., 2011).

d: The crystallite size is calculated based on the STEM images as shown in Figure S3 and Figure S6.

e: The defect density is calculated based on crystallite size in the parenthese.

Based on the estimate from the published two empirical formula models (Cançado et al., 2006; Zhong et al., 2014; Cancado et al., 2011), it is clear that the defect density of the synthesized h-NCs is ~5 times higher than that of the XC-72 carbon. After Pt deposition, the defect density of the 1.0 wt.% Pt_1/h-NC SAC is significantly decreased in comparison to pure h-NCs. Since the density of the Pt particles in the 1.0 wt.% nano-Pt/h-NC is extremely low, the defect density is only decreased by 4% due to Pt deposition, in comparison to pure h-NCs.

Transparent Methods

Preparation of single atom catalysts

Single Pt atoms were dispersed onto, via an adsorption method (Qiao et al., 2015; Lou et al., 2017; Lou et al., 2017), the surfaces of commercial carbon black (Vulcan XC-72) and home-made hollow nanocarbons (h-NCs). The precursors of Pt were hexachloroplatinic acid (Sigma-Aldrich).

1) Preparation of h-NCs. The h-NCs were synthesized via catalytic reforming/decomposition of ethanol on the surfaces of the ZnO nanowires. The details of synthesizing ZnO nanowires are discussed in the (Xu and Liu, 2016). In this work, we used the ZnO nanowires as templates to synthesize mesoporous h-NCs. The pre-formed ZnO nanowires were loaded into a high temperature furnace tube, which was then heated to 500 ^{o}C. A mixture of nitrogen, water and ethanol was then introduced into the furnace tube. Ethanol reforming as well as decomposition occurs on the surfaces of the ZnO nanowires. Such catalytic reactions result in residues of carbonaceous species uniformly coating the ZnO nanowires. Because of this coking induced deactivation, the thickness of the deposited carbonaceous layers is self-limiting. By controlling the reaction time, one can control the thickness of the deposited carbonaceous layers. After the desired thickness of the carbonaceous layers was obtained the ZnO (nanowires) were evaporated at a temperature of 750 ^{o}C for 6 h with a flowing gas mixture of H_2/Ar to produce the hollow carbon tubes with mesopores on the sidewalls.

2) Pt_1/h-NC preparation. The h-NCs were firstly dispersed in the ethanol and then the corresponding Pt precursors were slowly dropped into the ethanol. After being stirred at room temperature for 2 hours, the ethanol was slowly evaporated off and then the obtained precipitates were dried at 60 ^{o}C for 12 hours in air without further calcination. The actual Pt loading is 0.93 wt.% by ICP-MS.

3) Pt_1/XC-72 preparation. The carbon black powders (Vulcan XC-72) were firstly dispersed in the ethanol and then the corresponding Pt precursors were slowly dropped into the ethanol. After being stirred at room temperature for 2 hours, the ethanol was slowly evaporated off and then the obtained precipitates were dried at 60 ^{o}C for 12 hours in air. The actual Pt loading is 0.08 wt.% by ICP-MS.

4) Nano-Pt/h-NC preparation. The h-NC supported Pt nano particle catalyst (nano-Pt/h-NC) was prepared as control catalyst. The corresponding Pt precursors were firstly reduced by the $NaBH_4$ to form nano-meter sized Pt particles and then the above solution was slowly dropped into the ethanol to mix with the pre-synthesized h-NCs. After being stirred at room temperature for 2 hours, the ethanol was slowly evaporated off and then the precipitates were dried at 60 ^{o}C for 12 hours in air without further calcination. The actual Pt loading is 0.84 wt.% by ICP-MS.

Evaluation of the catalytic performance

The hydrogenation of 3-nitrostyrene was conducted in a Parr reactor. Before the activity test, the catalyst was first put into the reactor, to which 8 ml ethanol was added, and then the reactor was charged with 5 bar hydrogen and heated at 40 °C for 40 min to allow for the reduction treatment of the catalyst. After that, the 3-nitrostyrene substrate, internal standard O-xylene and 8 ml ethanol, were put into the reactor. Then, the reactor was flushed with 5 bar hydrogen for 11 times. After being sealed, the autoclave was charged with H_2 until 5 bar, then it was heated to 40 °C under stirring to initiate the reaction. The molecular ratio of Pt atoms to 3-nitrostyrene molecules is 0.078%. After reaction, the products were analyzed by gas chromatography (Agilent GC 7890A with HP-5 column) equipped with the Agilent auto sampler. The peaks were calibrated by the standard chemicals from Sigma-Aldrich. The turnover number (TON) value was measured by keeping the substrate conversion below 25% by tuning the molecular ratio of Pt atoms to 3-nitrostyrene molecules and the corresponding TON was calculated based on the total Pt loading in the catalyst, and the yields at the corresponding low conversion rate.

Catalyst Characterization

The loading level of the Pt was measured by a ThermoFinnegan iCAP Q quadrupole ICP-MS with CCT (Collision Cell Technology). Samples were run in KED (Kinetic Energy Discrimination) mode, with in-line aspiration of a multi-element internal standard.

Sub-angstrom resolution high-angle annular dark-field (HAADF) scanning transmission electron microscopy (STEM) images were obtained on a JEM-ARM200F TEM/STEM with a guaranteed resolution of 0.08 nm. Before microscopy examination, the catalyst powders were ultrasonically dispersed in ethanol and then a drop of the solution was put onto a copper TEM grid coated with a thin lacey carbon film.

The X-ray photoelectron spectroscopy (XPS) investigation was conducted on a Vacuum Generators 220i-XL using a mono-chromated Al Kα X-ray source (1486.6 eV). The samples were mounted onto the double-sided adhesive tape on the sample holder. The XPS spectra of the selected elements were measured with the constant analyzer pass energy of 20.0 eV. All binding energies (BEs) were referred to the C 1s peak (284.6 eV). The deconvolution protocol of the spectra is similar to our previous work (Lou et al., 2014; Lou et al., 2014). Raman experiments were conducted on LabRam HR 800 using 532 nm laser. The deconvolution protocol of the spectra was similar to that reported in literature (Wen et al., 2017).

The BET surface areas were measured by nitrogen adsorption at liquid nitrogen temperature by using a surface area and porosity analyzer (Quantachrome NOVA 4000e apparatus). Before measurement, the samples were degassed at 180 °C for 6 h in vacuum.

Supplemental References

Cancado, L. G., Jorio, A., Ferreira, E. H., Stavale, F., Achete, C. A., Capaz, R. B., Moutinho, M. V., Lombardo, A., Kulmala, T. S., and Ferrari, A. C. (2011). Quantifying defects in graphene via Raman spectroscopy at different excitation energies. Nano Lett. *11 (8)*, 3190-3196.

Chen, J. H., Cullen, W. G., Jang, C., Fuhrer, M. S., and Williams, E. D. (2009). Defect scattering in graphene. Phys. Rev. Lett. *102 (23)*, 236805.

Chernyak, S. A., Ivanov, A. S., Maslakov, K. I., Egorov, A. V., Shen, Z., Savilov, S. S., and Lunin, V. V. (2017). Oxidation, defunctionalization and catalyst life cycle of carbon nanotubes: a Raman spectroscopy view. Phys. Chem. Chem. Phys. *19 (3)*, 2276-2285.

Gopinadhan, K., Shin, Y. J., Yudhistira, I., Niu, J., and Yang, H. (2013). Giant magnetoresistance in single-layer graphene flakes with a gate-voltage-tunable weak antilocalization. Phys. Rev. B *88 (19)*, 195429.

Lou, Y., and Liu, J. (2017). A highly active Pt-Fe/gamma-Al_2O_3 catalyst for preferential oxidation of CO in excess of H_2 with a wide operation temperature window. Chem. Commun. *53*, 9020-9023.

Lou, Y., and Liu, J. (2017). CO Oxidation on Metal Oxide Supported Single Pt atoms: The Role of the Support. Ind. Eng. Chem. Res. *56*, 6916-6925.

Lou, Y., Cao, X. M., Lan, J., Wang, L., Dai, Q., Guo, Y., Ma, J., Zhao, Z., Guo, Y., Hu, P., and Lu, G. (2014). Ultralow-temperature CO oxidation on an In_2O_3-Co_3O_4 catalyst: a strategy to tune CO adsorption strength and oxygen activation simultaneously. Chem. Commun. *50*, 6835-6838.

Lou, Y., Ma, J., Cao, X., Wang, L., Dai, Q., Zhao, Z., Cai, Y., Zhan, W., Guo, Y., Hu, P., Lu, G., and Guo, Y. (2014). Promoting Effects of In_2O_3 on Co_3O_4 for CO Oxidation: Tuning O_2 Activation and CO Adsorption Strength Simultaneously. ACS Catal. *4*, 4143-4152.

Maldonado, S., Morin, S., and Stevenson, K. J. (2006). Structure, composition, and chemical reactivity of carbon nanotubes by selective nitrogen doping. Carbon, *44 (8)*, 1429-1437.

Ono, L. K., Yuan, B., Heinrich, H., and Cuenya, B. R. (2010). Formation and Thermal Stability of Platinum Oxides on Size-Selected Platinum Nanoparticles: Support Effects. J. Phys. Chem. C *114 (50)*, 22119-22133.

Peng, J., Chen, N., He, R., Wang, Z., Dai, S., and Jin, X. (2017). Electrochemically Driven Transformation of Amorphous Carbons to Crystalline Graphite Nanoflakes: A Facile and Mild Graphitization Method. Angew. Chem. Int. Ed. *56 (7)*, 1751-1755.

Peuckert, M., and Bonzel, H. P. (1984). Characterization of oxidized platinum surfaces by X-ray photoelectron spectroscopy. Surf. Sci. *145* (1), 239-259.

Prawer, S., Nugent, K. W., Jamieson, D. N., Orwa, J. O., Bursill, L. A., and Peng, J. L. (2000). The Raman spectrum of nanocrystalline diamond. Chem. Phys. Lett. *332* (1-2), 93-97.

Smith, M. W., Dallmeyer, I., Johnson, T. J., Brauer, C. S., McEwen, J. S., Espinal, J. F., and Garcia-Perez, M. (2016). Structural analysis of char by Raman spectroscopy: Improving band assignments through computational calculations from first principles. Carbon, *100*, 678-692.

Wang, L., Sofer, Z., Bousa, D., Sedmidubsky, D., Huber, S., Matejkova, S., Michalcova, A., and Pumera, M. (2016). Graphane Nanostripes. Angew. Chem. Int. Ed., *55 (45)*, 13965-13969.

Wen, G., Wang, B., Wang, C., Wang, J., Tian, Z., Schlogl, R., and Su, D. S. (2017) Hydrothermal Carbon Enriched with Oxygenated Groups from Biomass Glucose as an Efficient Carbocatalyst. Angew. Chem. Int. Ed. *56* (2), 600-604.

Wen, G., Wu, S., Li, B., Dai, C., and Su, D. S. (2015). Active sites and mechanisms for direct oxidation of benzene to phenol over carbon catalysts. Angew. Chem. Int. Ed. *54 (13)*, 4105-4109.

Xu, J., and Liu, J. (2016). Facet-Selective Epitaxial Growth of δ-Bi_2O_3 on ZnO Nanowires. Chem. Mater. *28*, 8141-8148.

Yan, X., Duan, P., Zhang, F., Li, H., Zhang, H., Zhao, M., Zhang, X., Xu, B., Pennycook, S. J., and Guo, J. (2019). Stable single-atom platinum catalyst trapped in carbon onion graphitic shells for improved chemoselective hydrogenation of nitroarenes. Carbon *143*, 378-384.

Zhang, X., Guo, J., Guan, P., Liu, C., Huang, H., Xue, F., Dong, X., Pennycook, S. J., and Chisholm, M. F. (2013). Catalytically active single-atom niobium in graphitic layers. Nat. Commun. *4*, 1924.

Zhong, J. H., Zhang, J., Jin, X., Liu, J. Y., Li, Q., Li, M. H., Cai, W., Wu, D. Y., Zhan, D., and Ren, B. (2014). Quantitative correlation between defect density and heterogeneous electron transfer rate of single layer graphene. J. Am. Chem. Soc. *136 (47)*, 16609-16617.